Published in Metrologia 55, issue 3, 366-385, 2018
which should be used for any reference to this work

First uncertainty evaluation of the FoCS-2 primary frequency standard

A Jallageas[1], L Devenoges[2], M Petersen[3], J Morel[1], L G Bernier[1], D Schenker[2], P Thomann[2] and T Südmeyer[2]

[1] Photonics, Time and Frequency Laboratory, Federal Institute of Metrology METAS, 3003 Bern-Wabern, Switzerland
[2] Laboratoire Temps-Fréquence, Institut de Physique, Université de Neuchâtel, Avenue de Bellevaux 51, 2000 Neuchâtel, Switzerland
[3] FEMTO-ST, CNRS, 32 Avenue de l'Observatoire, 25044, Besançon Cedex, France

E-mail: antoine.jallageas@metas.ch

Abstract

We report the uncertainty evaluation of the Swiss continuous primary frequency standard FoCS-2 (Fontaine Continue Suisse). Unlike other primary frequency standards which are working with clouds of cold atoms, this fountain uses a continuous beam of cold caesium atoms bringing a series of metrological advantages and specific techniques for the evaluation of the uncertainty budget. Recent improvements of FoCS-2 have made possible the evaluation of the frequency shifts and of their uncertainties in the order of 1×10^{-15}. When operating in an optimal regime a relative frequency instability of $8 \times 10^{-14}(\tau/s)^{-1/2}$ is obtained. The relative standard uncertainty reported in this article, 1.99×10^{-15}, is strongly dominated by the statistics of the frequency measurements.

Keywords: atomic clocks, primary frequency standards, continuous atomic fountain, caesium

(Some figures may appear in colour only in the online journal)

1. Introduction

Currently, realization of the SI second is made with primary frequency standards (PFSs) based on laser-cooled caesium (Cs) fountains operating in the pulsed cyclic mode [1–7]. The continuous Cs fountain FoCS-2 employs an alternative operating mode by using a continuous flux of cold atoms. FoCS-2 was developed by the Time and Frequency Laboratory of the University of Neuchâtel in collaboration with the Federal Institute of Metrology (METAS). Based on research that began in 1999 at the Observatory of Neuchâtel with the development of a continuous source of cold atoms [8] and on an experimental continuous fountain [9, 10], two continuous fountain clocks have been developed: a continuous fountain clock called FoCS-1 [11, 12] and, in 2006, a second version of the fountain with higher atomic flux [13, 14] called FoCS-2. This way of realizing the atomic second in a continuous PFS offers several advantages. Firstly, the continuous interrogation of FoCS-2 cancels the Dick effect limitation [15] offering a short-term stability of $< 1 \times 10^{-13}$ @ 1 s even when using a standard performance local oscillator as shown in figure 1. Another advantage is a lower atomic density as compared with that of a pulsed fountain for a given average atomic flux [11]. Finally, FoCS-2, with its continuous beam of cold atoms, increases the diversity of Cs fountains.

Having a continuous flux of atoms implies using an atomic beam with a parabolic trajectory (latus rectum: 2.576 mm) and interrogating the atoms using a microwave cavity with two distinct interaction zones. A light trap [12, 16] is also necessary to protect the atoms from parasitic light emanating from the source chamber.

For the last few years, we have worked on the characterization of the accuracy and on the improvement of the stability of FoCS-2, located at METAS. Recently, the FoCS-2 system has undergone several major modifications that enabled the evaluation of the PFS at the 10^{-15} level.

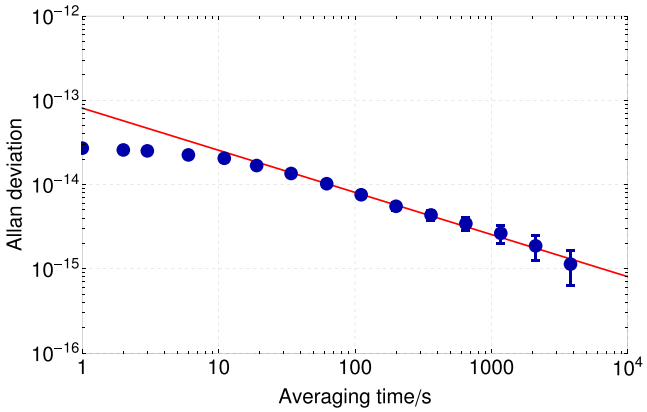

Figure 1. Typical Allan deviation of the frequency difference between FoCS-2 and the METAS hydrogen maser ID 1405701. The short-term stability at 1 s is 8×10^{-14}.

In this paper we report the first uncertainty evaluation of the Swiss PFS FoCS-2. Section 2 gives a complete description of the clock, and section 3 describes the operation of the fountain. Then, in section 4, we present the results of the evaluation of FoCS-2 frequency shifts. Finally section 5 discusses the uncertainty budget.

2. Description of the fountain

2.1. Atomic fountain

Figure 2 shows the main parts of the physics package of FoCS-2. The vacuum system can be divided into four different parts: the two-dimensional magneto-optical trap (2D-MOT) chamber, the source chamber, the free-flight chamber and the detection chamber. The vacuum system is made of aluminium, except for the 2D-MOT chamber, which is a flat wall glass cell glued to a titanium half nipple. An extra chamber (dome) located above the free-flight chamber outside the magnetic shields is made of 316L stainless steel. The system is pumped by a 65 l s^{-1} ion pump connected to the detection chamber at the bottom of the fountain and by a getter pump located in the dome above the free-flight chamber. The background pressure is 2×10^{-6} Pa next to the pumps. The ion pump is shielded with a 1.5 mm μ-metal layer to avoid magnetic perturbations.

All the laser beams are delivered by polarization-maintaining (PM) optical fibres from the optical table to different locations in FoCS-2.

In the 2D-MOT chamber [10], Cs atoms are collected from a Cs background vapour and initially cooled by the 2D-MOT. The magnetic field gradient is produced by four rectangular coils mounted directly on the 2D-MOT chamber. A laser beam is added along the trap direction to further increase the number of atoms. Atoms captured by the 2D-MOT are funnelled to a three-dimensional moving molasses (3D-MM).

The source chamber consists of four functional blocks—a 3D-MM (the fountain source), two 2D optical lattices (to collimate and to prepare the atomic states) and a depumping stage—while the detection chamber is only used for detection. As shown in figure 2, the source chamber and the detection chamber are located side by side and are separated by

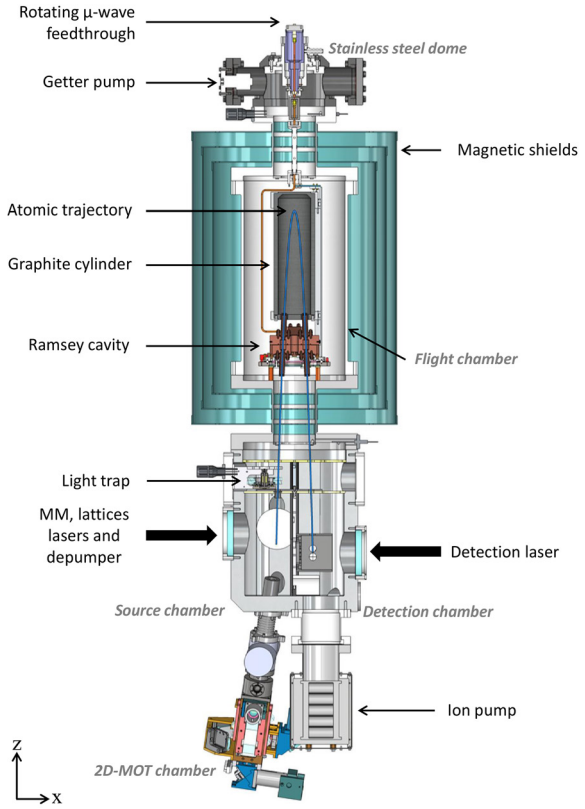

Figure 2. Sectional view of the FoCS-2 Cs fountain. There is an additional magnetic shield around the vacuum chamber not shown in this figure. FoCS-2 can be divided into four main parts: the 2D-MOT chamber, the source chamber, the free-flight chamber and the detection chamber.

an aluminium wall. Figure 3 shows a perspective view of the functional blocks inside the source chamber.

The moving molasses cooling stage uses large-diameter collimated beams delivered by the PM fibres. Due to technical constraints, the cooling beam geometry consists of a pair of horizontal beams created by one laser beam retro-reflected on a prism inside the vacuum chamber and of two upward and downward travelling pairs of counter-propagating laser beams, both making an angle of ±45° with the horizontal plane. The horizontal beams are located in the same plane as the atomic trajectory (0xz), while the upward and downward beams are located in the 0yz plane.

The next stages are two folded optical lattices, each consisting of a linearly polarized beam retro-reflected by a prism, as shown in figure 3. The first optical lattice is used to reduce the transverse temperature of the atomic beam while the second lattice is used for state preparation and to tilt the atomic beam to realize the parabolic trajectory. These two lattices are placed in a plane tilted by 2.6° with respect to the horizontal plane. The first optical lattice is placed 4 cm above the 3D-MM with the second optical lattice placed a further 2.5 cm above the first one. In order to perform a two-laser state preparation of the atoms, a second linearly polarized laser beam (pumping beam) is overlapped with the second lattice and is retro-reflected by a mirror in the same horizontal plane. We invite the reader to consult [17] for more details about the geometry of these optical lattices and about optical state

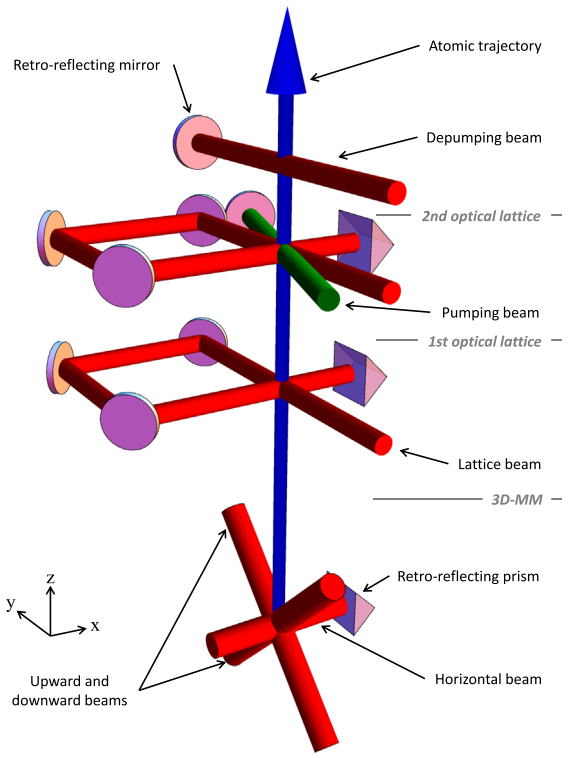

Figure 3. Schematic of the preparation stages inside the source chamber. From bottom to top: the 3D moving molasses, the two optical lattices and the depumping beam.

preparation by the two-laser method. A last laser beam is used to depopulate the hyperfine level $|F = 4\rangle$, and is located 2 cm above the state preparation and retro-reflected on a mirror placed outside of the vacuum chamber.

Scattered light from the cold atom preparation stages in the free-flight chamber introduces a significant frequency shift in the order of 10^{-12}. This effect is suppressed in pulsed fountains by turning the laser beams off during the free flight of the atoms. Here, this is not possible. To avoid this frequency shift while leaving the laser beams on, a light trap is used. The light trap is a velocity-selective turbine located 7 cm above the depumping beam, which blocks the photons scattered from the source and transmits 95% of atoms, having a velocity equal to the rotation speed of its blades. The light trap is driven by an electrostatic motor (ESM). The turbine is an assembly of 18 absorbing blades mounted at an angle of 45° on the rotor of the vacuum-compatible ESM. The light trap and the ESM are described in detail in [16] and [12]. The angular speed of the rotation is around 17 rotations per second, and wear of the bearings is a challenge for continuous operation. However, by optimizing the components (especially by using vacuum-compatible oil), the lifetime of the ESM in the light trap can become longer than two years. A photodiode is placed just at the exit of the light trap (23 cm above the 3D-MM) in order to measure residual scattered light coming from the atomic source. As described in section 4.6.1, this photodiode is used to evaluate the frequency shift coming from spurious light.

After leaving the cooling region and passing twice through the Ramsey cavity, the atoms fall down into the detection chamber. This chamber contains a graphite box that protects the atoms and the detection photodiode from stray light. The fluorescence produced by the interaction of the detection light with the atoms indicates the population of the $F = 4$ level. It is collected and focused onto a 1 cm^2 photodiode by two Fresnel lenses. The fluorescence collection efficiency is increased by a spherical mirror mounted on the internal wall separating the source and detection chambers. The centre of curvature coincides with the intersection between the atomic beam and the probe beam. The photocurrent is converted into a voltage signal by a transimpedance amplifier (1 GΩ) with a current noise spectral density of 10^{-14} A Hz$^{(-1/2)}$ at 1 Hz. Due to the large number of photons per atom detected by this set-up (see below, section 3), the dominant noise source limiting the short-term stability of the fountain is the atomic shot noise.

In order to control the magnetic field required for cooling the atoms and for defining a quantization axis for the state preparation, three orthogonal pairs of coils in a Helmholtz configuration are mounted outside the vacuum chamber, inside the outermost magnetic shield. Perturbing external fields are compensated for in order to get a resulting field of 1 μT and to align it with the polarization of the pumping laser beam used in the state preparation (see section 2.2).

The free-flight chamber is an aluminium cylinder located inside the magnetic shields, while the stainless steel dome is outside the magnetic shields. The inner walls of the free-flight chamber are partially coated with graphite paint to absorb spurious microwave background radiation.

The stainless steel dome with two half-nipples tops the free-flight chamber. The two half-nipples of the dome are used for connecting the getter pump and a pressure gauge. Two coaxial cables pass through a rotating feedthrough at the top of the dome. These two cables bring the interrogating microwave signal to the Ramsey cavity. The microwave cavity is placed on a rotating support connected to the rotating feedthrough by two aluminium rods allowing a rotation of the cavity by 180°. This is needed for the evaluation of the end-to-end phase shift (see section 4.4.3). In this way the cavity can be rotated manually from outside the vacuum chamber. The positions of the interaction regions are interchangeable and reproducible to within 0.02 mm. The microwave signal is split via a power divider located outside the vacuum chamber and it is carried to the two feeding ports of the microwave cavity by coaxial cables. The balance between these two arms is adjusted by a phase shifter and a tunable attenuator located on both outputs of the power divider. To do that, we use an interferometric technique which consists in cancelling the atomic signal. Once this step is achieved, a phase shift of π is set to optimize the atomic signal. This method leads to a balance better than 99%. All the components required for splitting and balancing the microwave signal are placed in an aluminium box that rotates with the rotating feedthrough. A graphite cylinder supported by two aluminium rods is positioned just above the cavity, between the coaxial cables and the atomic trajectory. As discussed in section 4.4.2, this cylinder shields the atoms from any spurious microwave field.

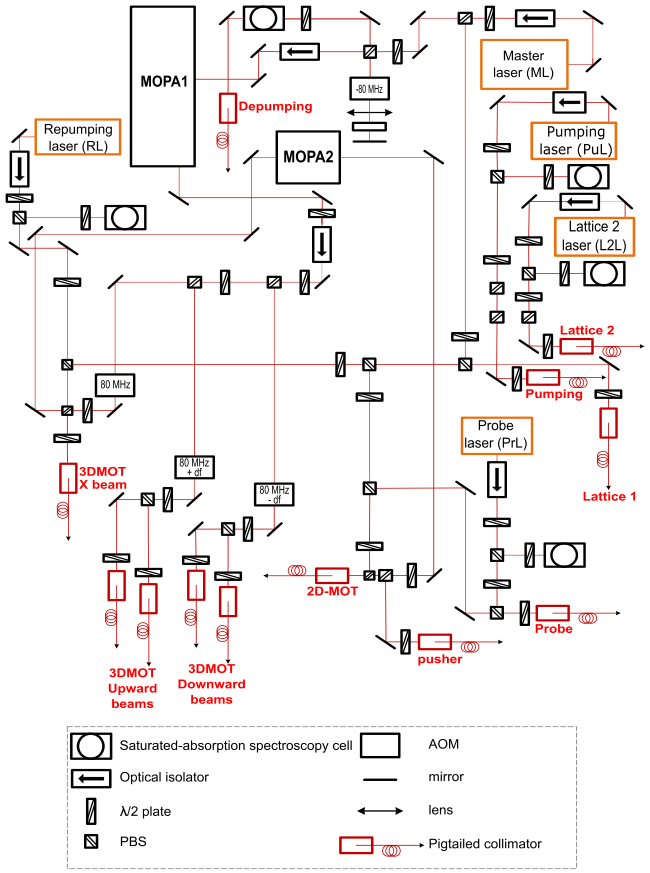

Figure 4. Simplified schematic of the optical set-up. The optical fibre couplers are connected to polarization-maintaining optical fibres which carry the light from the optical table to the fountain.

The free-flight chamber temperature is controlled by eight heating rods inserted in the top and bottom of the aluminium cylinder, outside of the cylindrical magnetic shields. The temperature inside the vacuum chamber is adjusted to 296.830 K by using the thermal radiation of the free-flight chamber, whose temperature is controlled by a feedback loop system allowing a thermal stability of ± 0.075 K.

The free-flight chamber is surrounded by three cylindrical 1.5 mm thick layers of μ-metal magnetic shields, which reduce the Earth's magnetic field to less than 2 nT inside the chamber. A fourth rectangular magnetic shield surrounds the whole fountain. The magnetic C-field used to lift the degeneracy of the hyperfine sublevels and to define the quantization axis in the cavity is created by a solenoid coil covering the inner surface of the innermost μ-metal shield. The 56.1 cm high cylindrical solenoid, 39.5 cm in diameter, is made up of 440 turns of copper wire. In order to have a good homogeneity of the C-field in the cylinder, independent triplets of axial coils are placed at both ends of the free-flight chamber.

The FoCS-2 fountain is placed on an orientable platform base, which allows adjustment of the verticality of the fountain set-up.

2.2. Lasers and optics

Figure 4 shows a simplified schematic of the optical set-up used to operate FoCS-2. This system, whose properties are summarized in table 1, consists of five lasers: the master laser (ML), the pumping laser (PuL), the lattice 2 laser (L2L), the probe laser (PrL), and the repumping laser (RL), complemented by two power amplifiers (MOPA1 and MOPA2). All the lasers required for laser cooling, atomic preparation, and detection operate on the Cs D_2 transition at 852 nm.

Table 1. Summary of the laser beams' main characteristics. The notation $\nu_{ij'}$ corresponds to $|F=i\rangle \rightarrow |F'=j\rangle$. Note that $\nu_{44'} + 240$ MHz$= \nu_{45'} - 12$ MHz and $\mathrm{d}f = 3.3$ MHz.

	Transition	Intensity, mW	Waist, mm
2D-MOT chamber			
2D-MOT	$\nu_{45'} - 12$ MHz	180	2.9
Rep. 2D-MOT	$\nu_{34'}$	1	2.9
Pusher	$\nu_{45'} - 12$ MHz	7.5	2.9
Source chamber			
3D-MM upward	$\nu_{45'} - 12 + \mathrm{d}f$ MHz	11	5.75
3D-MM downward	$\nu_{45'} - 12 - \mathrm{d}f$ MHz	11	5.75
3D-MM X	$\nu_{45'} - 12$ MHz	11	5.75
Rep. 3D-MM X	$\nu_{34'}$	0.14	5.75
Lattice 1	$\nu_{44'} + 160$ MHz	8.5	2.84
Rep. lattice 1	$\nu_{34'}$	0.075	2.84
Lattice 2	$\nu_{44'-45'}$	2.2	2.84
Pumping	$\nu_{32'-34'}$	0.25	2.84
Depumping	$\nu_{44'}$	0.56	2.84
Detection chamber			
Probe	$\nu_{45'} - 2$ to 6 MHz	0.78	2.84

The ML is used to generate the cooling light. It is a commercial distributed feedback laser diode. The output power of the ML is 100 mW with a linewidth of 2 MHz. Its beam is split into three to produce the first optical lattice (transverse cooling), the input to the MOPA1 optical amplifier, and the depumping beam. The first two of those beams are stabilized at $+160$ MHz above the $|F=4\rangle \rightarrow |F'=4\rangle$ transition frequency, by double-passing through an acousto-optic modulator (AOM) and by using a saturated absorption signal in a Cs cell at room temperature. The depumping beam is stabilized to the $|F=4\rangle \rightarrow |F'=4\rangle$ transition and is used for depopulating $|F=4\rangle$. It is linearly polarized and has a power of 560 μW. The beam is collimated to a waist of 2.84 mm and is geometrically limited by a diaphragm to a diameter of 11 mm. The first optical lattice beam has the same dimensions as the depumping beam and a power of 8.5 mW. It is superimposed with a repumping beam (75 μW). The upward, horizontal and downward 3D-MM cooling beams are obtained by dividing the MOPA1 output (250 mW) into three beams. Their respective frequencies are shifted by $(+80 + \mathrm{d}f)$ MHz, $+80$ MHz and $(+80 - \mathrm{d}f)$ MHz by using three AOMs. The frequency difference $\mathrm{d}f$ determines the atom's launch velocity v_l according to $v_l = \sqrt{2} \times \lambda \times \mathrm{d}f$. All the laser beams used for the 3D-MM are in a lin.-perp.-lin. configuration with a power of 11 mW. The beams are collimated to a waist of 5.75 mm and are geometrically limited to a diameter of 30 mm. The horizontal beam is superimposed over a repumping beam with a power of 140 μW.

To optimize the 2D-MOT, a part of the horizontal beam coming from MOPA1 passes through a second optical amplifier, MOPA2. The power output of MOPA2 is 180 mW. Linear polarization is guaranteed by passage through two polarizing beam splitters (PBSs). The first PBS splits off 7.5 mW to

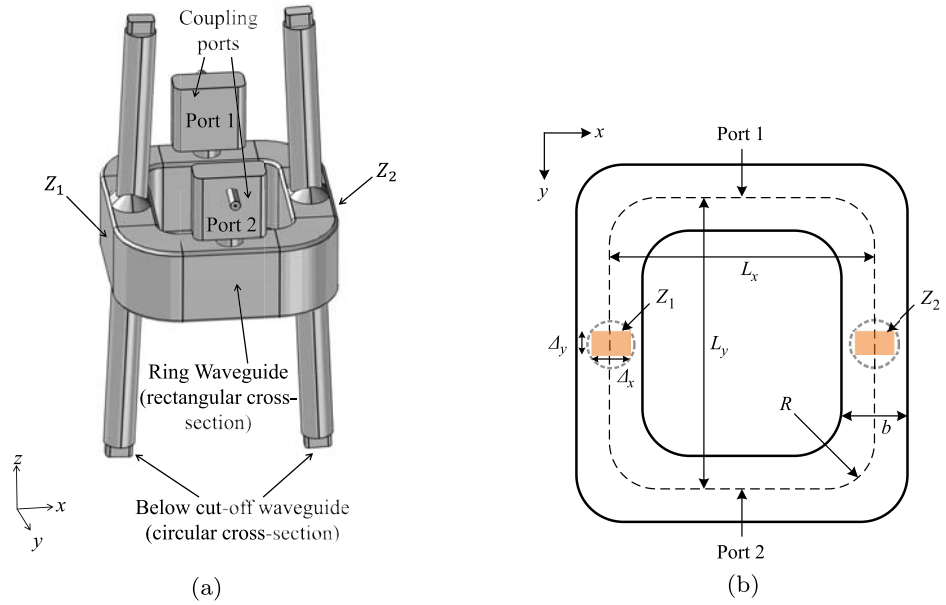

Figure 5. Schematics of the Ramsey cavity. (a) represents the inner volume of the cavity. The microwave signal is injected into the ring waveguide by two irises (8 mm diameter) connecting the coupling ports to the cavity. (b) shows the top view of the waveguide. The coloured rectangles represent the interaction zones and are placed at equal distances from the two ports. The dashed grey circles represent the diameters of the cutoffs. The cavity dimensions are $L_x = 56.2$ mm and $L_y = 61.77$ mm whereas the width of the waveguide is $b = 14.0$ mm and R, the bending radius, is equal to 17 mm.

generate the 2D-MOT pushing beam while the second PBS is used to superimpose the repumping beam with the cooling beam used in the 2D-MOT.

A two-laser optical pumping method is used for the atomic state preparation $|F = 3, m_F = 0\rangle$ [17]. The first beam is produced by the L2L tuned to the cross-over of the $|F = 4\rangle \rightarrow |F' = 4\rangle - |F = 4\rangle \rightarrow |F' = 5\rangle$ absorption line. With this set-up, atoms are pumped toward $|F = 3\rangle$ while being cooled to ~ 4 μK by a Sisyphus cooling method [18]. This beam is linearly polarized and has a power of 2.2 mW. The second beam is generated by the PuL and tuned on the $|F = 3\rangle \rightarrow |F' = 2\rangle - |F = 3\rangle \rightarrow |F' = 4\rangle$ cross-over. The PuL is an external-cavity diode laser (ECDL) in a Littrow configuration with a linewidth of 500 kHz. Its beam is linearly polarized and has a power of 250 μW. The two laser beams used for the two optical lattices and the pumping beam are collimated to a waist of 2.84 mm and geometrically limited to a diameter of 11 mm.

All the repumping beams are generated by the RL tuned to the $|F = 3\rangle \rightarrow |F' = 4\rangle$ transition. The power of each repumping beam is adjusted to 1% of the cooling beam power.

The probe light is generated by the PrL, which consists of an ECDL in a Littrow configuration locked to the $|F = 4\rangle \rightarrow |F' = 5\rangle$ absorption line in a Cs-saturated absorption cell. This line is red shifted by 2–6 MHz by applying a magnetic field to the cell. The PrL is circularly polarized to maximize the scattered intensity per atom by optical pumping to the 'bright' state $|F = 4, m_F = 4\rangle$. The red shift of the retro-reflected probe beam prevents the loss of atoms by recoil from the repeated photon scattering. The probe beam has a power of 870 μW and a linewidth smaller than 500 kHz. It is collimated to a waist of 5.68 mm and is geometrically limited to a diameter of 14 mm.

2.3. Microwave cavity

One of the main differences between pulsed fountains and FoCS-2 is the microwave cavity design. Since FoCS-2 uses a continuous atomic beam with a parabolic trajectory, the Ramsey cavity must have two interaction zones. The geometric parameters are reported in figures 5(a) and (b). The height of the ring waveguide cross-section is 24.9 mm and the width is 14 mm. The two interaction zones (Z_1 and Z_2) are at equal distances from the two feeding ports and have dimensions of $\Delta_x = 8$ mm and $\Delta_y = 5$ mm. Their sizes are determined by rectangular slits at the outer end of each below-cutoff waveguide. To avoid microwave leakage from the oxygen-free high-conductivity copper cavity, indium gaskets are used to assemble the upper and lower parts of the waveguide as well as the cutoffs (9.5 mm × 58.4 mm) and the coupling ports. The thickness of each half-part of the cavity is adjusted manually by polishing to achieve resonance at 9.192 631 770 GHz when the part's temperature is 296.83 K with a thermal coefficient of -150.804 kHz K^{-1}. Moreover each part has an internal roughness of 0.012 μm.

The microwave cavity of FoCS-2 is a TE_{105} ring waveguide cavity. Analysis of the behaviour of the microwave field is made with finite-element software COMSOL, solving Maxwell's equations numerically for the inner vacuum volume made with the boundary conditions imposed by the copper walls (conductivity $\sigma = 5.95 \times 10^7$ S m^{-1}). The achieved results are shown in figures 6 and 7. Note that in each simulation, the

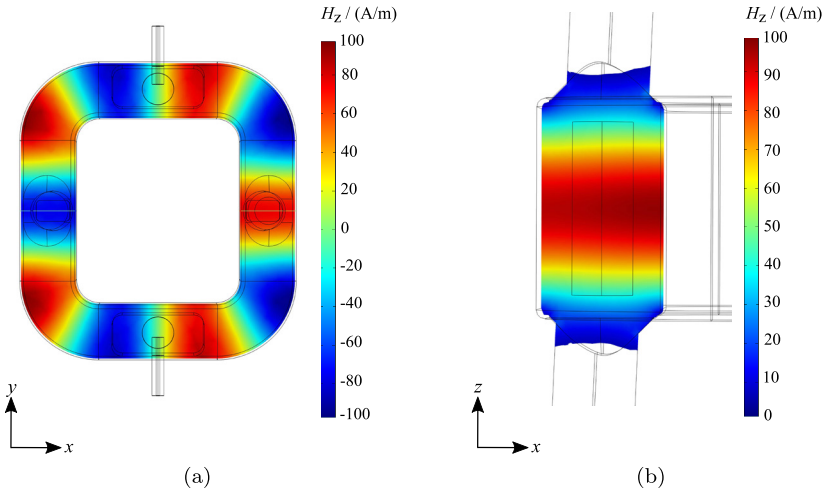

Figure 6. (a) Vertical component H_z of the TE_{105} mode in the cavity mid-plane. The fifth-order periodicity of TE_{105} is clearly visible in the horizontal plane (0xy). (b) Vertical slice through the centre of one of the two interaction zones. It shows the field distribution over this region and the penetration depth inside the below-cutoff waveguides. The strong attenuation effect of the cutoff is observable.

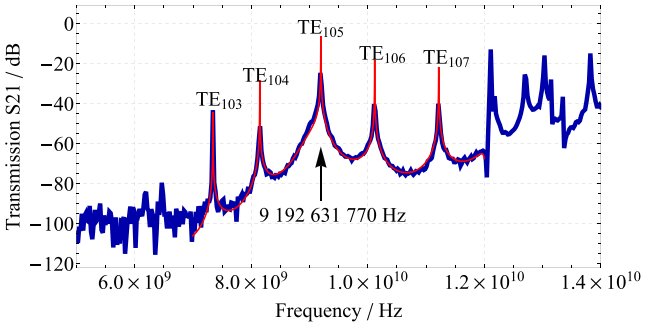

Figure 7. The cavity transmission spectrum. The blue curve corresponds to measurements made on the cavity while the red curve comes from the FEM simulations. The central peak at 9.192 631 770 GHz is the TE_{105} mode.

number of mesh elements is chosen to reduce numerical noise to a negligible level. Moreover the power injected into each coupling port is equal to that of the other. Figure 6(a) presents the vertical component H_z of the TE_{105} mode in the central horizontal plane of the cavity. We can observe the order-five periodicity of the TE_{105} mode and a π-phase difference between the two interaction zones. This difference has been shown to have metrological advantages [19–21]. Figure 6(b) is a blow-up of one of the interaction zones. It is thus possible to observe the efficiency of the attenuation of the field obtained with the cutoffs. This attenuation is experimentally measured to be better than 250 dB compared to the centre of the interaction zones.

Figure 7 shows a comparison of the cavity transmission spectrum obtained by finite-element analysis with that obtained by measurement. The graph shows the microwave signal transmitted to port P_2 while port P_1 is being excited with frequencies ranging from 6 GHz to 14 GHz. One can see in this graph that the simulation and experiment agree well. The closest resonances, TE_{104} and TE_{106}, are approximately 1 GHz away from the TE_{105} mode used to interrogate the atoms. This separation is sufficient to reduce off-resonance excitation of these modes to a negligible level. The loaded quality factor is $Q_C = 6900$.

The cavity is designed to have low mode density and small longitudinal and transverse phase variations across the atomic passages. Finite-element simulations are also used to predict the phase distribution in the cavity. The results are shown in figure 8 for the phase variations in the cavity mid-plane and in figure 9 for the longitudinal phase variations. Firstly, one observes that microwave power flows from the feeding ports to the walls, where it is dissipated due to the finite copper conductivity. Since the interaction zones are equidistant from the feeding ports, the resulting power flow in these regions is minimal. As a consequence, phase variations are minimized over the interaction zones compared to those in other regions of the waveguide. Moreover, one observes in fig 8(b) that the phase variations present a saddle structure over Z_1. Using the physical parameters for the copper conductivity and material permittivity given previously, we obtain a peak-to-peak phase variation of $\Delta\phi_{pp} \simeq 31$ µrad over the interaction zone in the cavity mid-plane. The simulated longitudinal phase variation in interaction zone Z_1 is shown in figure 9. According to [22], peak-to-peak variations are larger along the optimal atomic trajectory. For this specific design, we get 100 µrad inside the waveguide cavity and 250 µrad considering the phase up to 3 mm inside the cutoff waveguide, which is about seven times that in the horizontal plane. However, previous work [23] shows that their importance in the frequency shift is smaller than that of mid-plane variations and they are weighted in our case by the ten-fold decrease of the amplitude H_z of the electromagnetic field. This assumption is confirmed by Monte Carlo simulations. Indeed, solving the Bloch equations in the computed field, we find that the frequency shift due to phase variation is below 10^{-15} for 95% of the trajectories and below 2×10^{-15} for 99.7% of them. Averaging these results leads to an average shift smaller than 10^{-15}.

Note that these phase simulations are used in Monte Carlo computations of the clock frequency, whose aim is to make comparisons with the results of measurement (section 4.4.4).

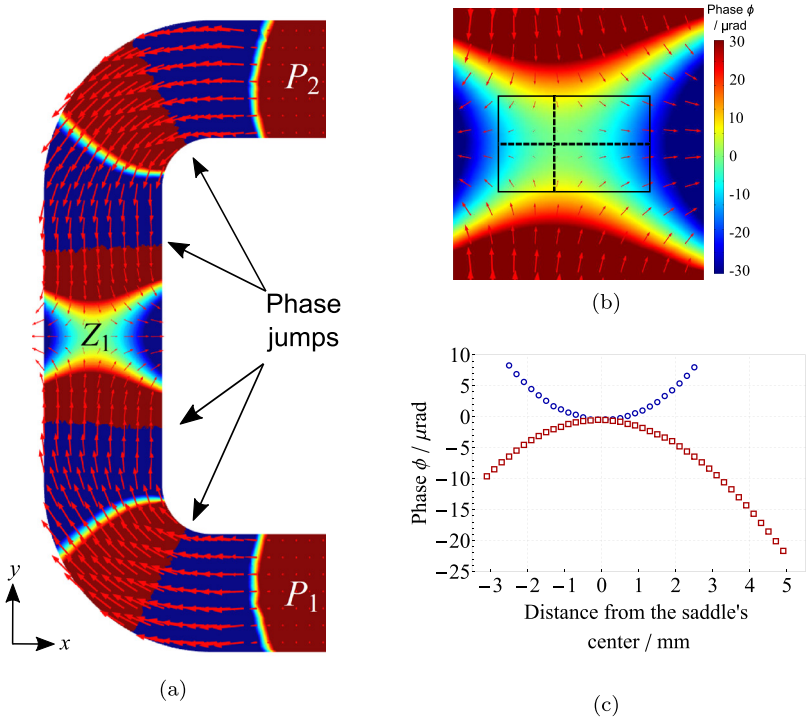

Figure 8. Analysis of the transverse phase gradient. (a) shows the phase variation that occurs in half of the cavity in the horizontal plane 0xy. The arrows show the time-averaged power flow (Poynting vector) due to losses in the waveguide walls. Phase variations are smaller in the interaction zone than in other regions of the waveguide where the power flow is more important. Please note that uniform dark blue corresponds to zones where the phase value is smaller than -30 µrad. Similarly, uniform dark brown corresponds to zones where the phase value is higher than $+30$ µrad. (b) is an enlargement of interaction zone Z_1. The density plot shows phase variations in the cavity mid-plane with a full scale of ± 30 µrad. (c) shows the behaviour of the phase along the two (0x and 0y) dashed lines in figure (b). The phase variation presents a saddle structure and the phase at the centre of the saddle is arbitrarily set to 0.

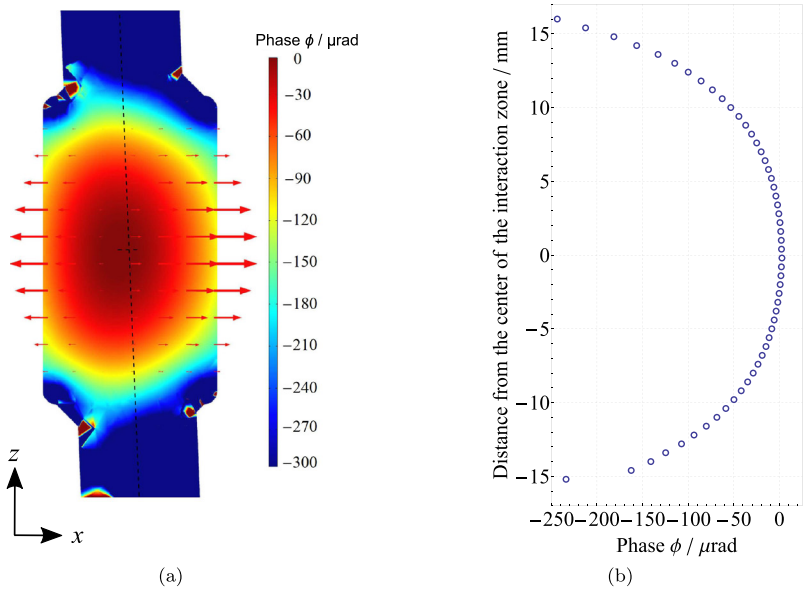

Figure 9. Analysis of the longitudinal phase gradient. (a) shows the phase variation that occurs in an interaction zone in the same vertical plane 0xz as the atomic beam. The red arrows show the time-averaged power flow (Poynting vector) due to losses in the waveguide walls. (b) shows the behaviour of the phase along the dashed line in figure (a), which corresponds to the average atomic trajectory. The phase at the centre of the interaction zone is arbitrary set to 0.

2.4. Microwave synthesizer

FoCS-2 uses a commercial microwave synthesizer. Four internal oscillators (a 5 MHz voltage-controlled crystal oscillator (VCXO), a 100 MHz VCXO, a 9.2 GHz dielectric resonator oscillator (DRO), and a 7.368 23 MHz signal from a direct digital synthesizer (DDS)) are successively phase-locked to the external reference signal from a hydrogen maser [24, 25]. The DRO and DDS signals are mixed to produce the 9.192 631 770 GHz clock transition frequency.

3. Operation of the fountain

The FoCS-2 fountain operates in a continuous mode. The atoms follow the same series of successive manipulation steps and all these steps are performed continuously. The steps are:

- pre-cooling and trapping in the 2D-MOT to produce a slow beam,
- capture of the slow beam, cooling and launching into the 3D-MM,
- transverse cooling and state selection in the two optical lattices,
- Ramsey interrogation in the microwave cavity during the ballistic flight,
- detection.

The 2D-MOT is loaded from a Cs vapour. Slow atoms ($v < 20$ m s^{-1}) are channelled by the 2D-MOT and the resulting slow beam is used to load the 3D-MM with a flux of 1×10^{10} atoms s^{-1}. To optimize the atomic flux the magnetic field gradient is set to 1.15×10^{-2} T m^{-1}. In the 3D-MM the atoms are simultaneously cooled further and launched upwards. The vertical velocity is controlled by the frequency difference between the up- and down-oriented optical beams of the 3D-MM. The 3D-MM has a typical flux of 1×10^9 atoms s^{-1} for an optimal velocity of 3.98 m s^{-1}.

In order to obtain a parabolic trajectory, a small horizontal kick is applied to the atoms passing through the first optical lattice beam, which is tilted by 1.6° with respect to the horizontal plane. The two optical lattices decrease the transverse atomic temperature from 80 μK to 4 μK. The longitudinal temperature is not affected and remains at 80 μK. State preparation is made in the second optical lattice where an optical beam is added to transfer atoms to $|F = 3, m_F = 0\rangle$ (two-laser method [17]). The state preparation efficiency is about 60%. The atoms remaining in the $|F = 4\rangle$ sublevels are depumped to $|F = 3\rangle$ by a last optical beam (depumping beam). Then the atoms pass through the rotating light trap while the light coming from the source chamber is blocked. The light trap turns with a frequency of 17 Hz. In order to optimize the cooling efficiency and the state preparation the Helmholtz coils generate a vertical magnetic field of 1 μT in the cooling and detection chambers. The C-field is adjusted to 71.4 nT, which sets the frequency difference between the Zeeman sublevels $m = 0$ and $m = \pm 1$ to 240 Hz.

The atoms complete the Ramsey interaction after passing through the two interaction areas of the microwave cavity and fall down into the detection chamber. Figure 10 shows the measured Ramsey fringes. In order to maximize the transition probability between $|F = 3, m_F = 0\rangle$ and $|F = 4, m_F = 0\rangle$ the microwave power is adjusted using the Rabi oscillations in figure 11. By choosing the power corresponding to the first maximum, the atoms experience two $\pi/2$ pulses, one during the rising part of the trajectory through the first interaction zone and a second one during the falling part of the trajectory through the second interaction zone of the Ramsey cavity. At optimal velocity the atomic apogee is 0.32 m above the centre of the microwave cavity.

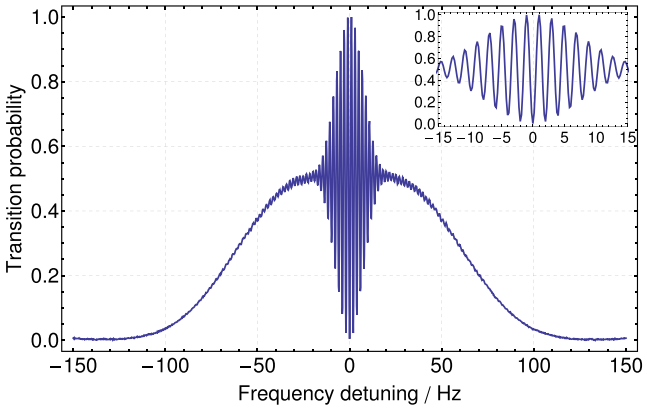

Figure 10. Ramsey fringes of FoCS-2 with a frequency step of 0.2 Hz, each point being the average of the atomic signal at 1.04 s. The low number of fringes compared to that of pulsed fountain clocks is due to the higher longitudinal temperature of the atomic beam. The dark central fringe is due to a phase difference of 180° between the two Ramsey interaction zones.

The atomic flux is 4×10^6 atoms s^{-1} in the $|F = 4, m_F = 0\rangle$ atomic state in the detection chamber. Atoms in $|F = 4\rangle$ are detected by the probe beam. The emitted signal corresponds to about 8000 photons/atom collected with an efficiency of 3%. The fountain clock microwave interrogation signal is produced by square-wave modulation of the phase of the 9.192 631 770 GHz signal probing the atoms. The $f_m = 0.96$ Hz phase modulation frequency is controlled by the reference output of a digital lock-in amplifier (DLA) [15]. The detection signal from the photodiode is demodulated in the DLA to produce the servo-loop error signal. The error is integrated with a pi filter and frequency corrections δf are directly applied to the synthesizer through the DDS via a LabVIEW software routine (National Instruments Corp.) with a resolution of 1 μHz. Figure 12 shows a schematic of the frequency feedback loop.

4. Evaluation of systematic effects

In this section we report the evaluation of the most important effects which induce frequency shifts in FoCS-2 and their associated uncertainties. These uncertainties are standard uncertainties ($k = 1$).

4.1. Second-order Zeeman shift

Evaluation of the second-order Zeeman shift requires precise knowledge of the magnetic field in the free-flight zone. In the case of pulsed fountains, the methods developed to measure the magnetic field in the resonator are based on launching balls of atoms at different altitudes. This is not applicable to a continuous fountain since the atomic trajectory is not strictly vertical and therefore the launching velocity is constrained by the geometry of the set-up. In [26] we show that one can retrieve the time-averaged magnetic field $\overline{B}(T)$ and deduce the second-order Zeeman shift by time-resolved Zeeman spectroscopy. The basic idea is to measure the Zeeman frequency

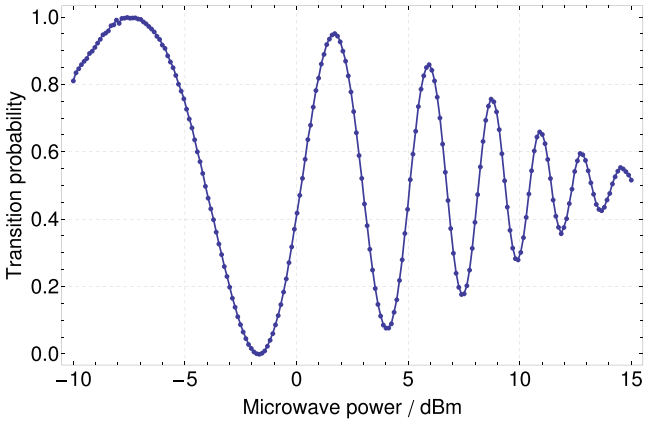

Figure 11. Typical Rabi oscillations of FoCS-2 as a function of the output power of the microwave synthesizer. The power scanning step is 0.12 dB. The first maximum is chosen as the power value to perform a $\pi/2$ pulse.

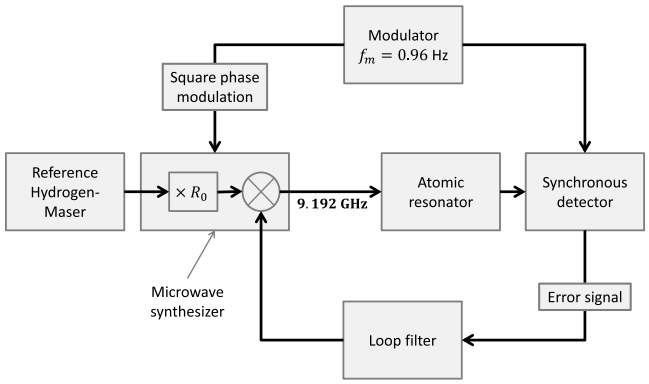

Figure 12. Schematic of the frequency feedback loop used to operate FoCS-2.

profile by exciting $\Delta F = 0, \Delta m_F = \pm 1$ transitions. Precise knowledge of the transit times [27] allows one to compute the spatial magnetic field profile and finally, by numerical averaging along the atomic trajectory, to obtain the time-averaged magnetic field probed by the atoms in the free-evolution zone. Figure 13 shows the resulting time-averaged magnetic field in the continuous fountain around the optimal transit time.

As discussed in [26], the evaluation of the Zeeman shift is affected by the uncertainty on the magnetic field measurement. There are two contributions to the uncertainty. The first one is due to the measurement of $(\overline{B}(T))^2$ instead of $\overline{B^2}(T)$. The second contribution, which is the dominant one, comes from the uncertainties of the magnetic field measurements and from the numerical processing. The evaluation also takes into account the uncertainty due to the long-term evolution of the magnetic field. The normalized second-order Zeeman shift and the associated uncertainty are:

$$\frac{\Delta\nu_{\mathrm{Z}}}{\nu_0} = (23.59 \pm 0.21) \times 10^{-15}.$$

4.2. Relativistic effects

4.2.1. Gravitational shift. When making comparisons between clocks at the global level, the time reference Terrestrial Time

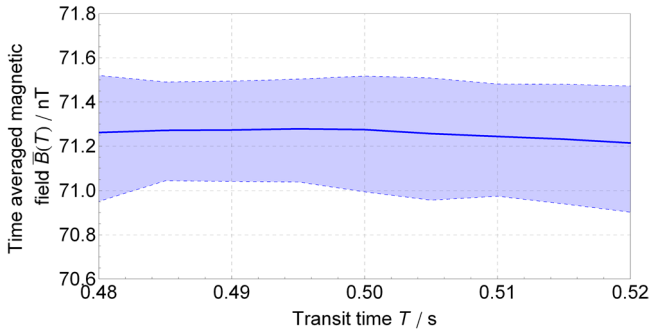

Figure 13. Time-averaged magnetic field along the atomic trajectory as a function of the transit time T. The blue solid line is determined by numerical integration of the spatial profile of the magnetic field $B(z)$. The blue dashed lines represent the $\pm 1\sigma$ error band on the atomic velocity distribution.

(TT) is used. TT is constructed from Geocentric Coordinate Time. As long as uncertainty better than 10^{-17} on frequency comparisons for clocks on Earth is not possible, it is easier to estimate the relativistic shift as if it were directly compared with a clock on the rotating geoid [28].

FoCS-2 is located at METAS in Bern about 550 m above the local rotating geoid. At this altitude the effect of the gravitational potential on the clock frequency is estimated by [29]:

$$\frac{\Delta\nu_{\mathrm{G}}}{\nu_0} = \frac{g \times h}{c^2}, \tag{1}$$

where $g = 9.805\,884 \pm 0.000\,002$ m s^{-2} is the local gravitational acceleration corrected for the centrifugal acceleration and h is the time-averaged altitude of the atoms above the cavity relative to the rotating geoid. The altitude of FoCS-2 is measured relative to an absolute Swiss reference point located at METAS. This altitude is converted into the height above the modelled EGM2008 geoid using the REFRAME online service from the Swiss Federal Office of Topography and the International Centre for Global Earth Models website. Therefore $h = 547.4 \pm 0.2$ m. The EGM2008 value near Bern is estimated to have an uncertainty smaller than 20 cm. Thus, the relativistic shift due to the altitude difference between the FoCS-2 laboratory and the rotating geoid is:

$$\frac{\Delta\nu_{\mathrm{G}}}{\nu_0} = (59.72 \pm 0.02) \times 10^{-15}.$$

4.2.2. Second-order Doppler shift. Beyond the relative position of FoCS-2 to the rotating geoid, the second-order Doppler frequency shift occurs because the atoms are moving with respect to the Ramsey cavity. The frequency shift is due to the time dilation between a moving clock and one which is stationary in the reference frame of the laboratory and can be calculated as [29]:

$$\frac{\Delta\nu_{\mathrm{D}}}{\nu_0} = -\frac{v_{\mathrm{rms}}^2}{2c^2}, \tag{2}$$

where v_{rms} is the average velocity of the atoms between the two interrogation zones and c is the speed of light in vacuum. In FoCS-2, $v_{\mathrm{rms}} = (1.49 \pm 0.03)$ m s^{-1}; thus the second-order Doppler shift and the associated uncertainty are:

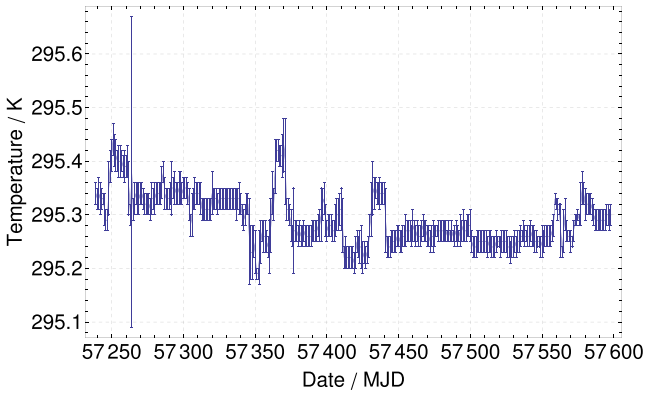

Figure 14. Evolution of the temperature of the FoCS-2 laboratory in one year.

$$\frac{\Delta\nu_{\mathrm{D}}}{\nu_0} = (-0.012 \pm 0.001) \times 10^{-15}.$$

4.3. Blackbody radiation (BBR) shift

If the atomic beam is exposed to electromagnetic radiation in the interaction zone, coupling between the atoms and an oscillating magnetic field (an electric field) during their ballistic flight will produce a second-order Zeeman shift (a second-order Stark shift). Therefore, if the temperature of the device is not 0 K, the frequency of the primary standard must be corrected for the BBR shift [30]. Indeed, the total perturbation is dominated by the AC Stark shift, which can be associated with the radiation of a blackbody radiator at the temperature of the vacuum enclosure [29, 31–33]. The related frequency shift is given by:

$$\Delta\nu_{\mathrm{BBR}} = k_0 E_{T_0}^2 \left(\frac{T_{\mathrm{F}}}{T_0}\right)^4 \left[1 + \epsilon \left(\frac{T_{\mathrm{F}}}{T_0}\right)^2\right], \qquad (3)$$

where $k_0 = -2.282(4) \times 10^{-10}$ Hz $(\mathrm{V\ m^{-1}})^{-2}$ is the DC scalar polarizability of the clock transition [34–37], $E_{T_0} = 831.9\,\mathrm{V\ m^{-1}}$ is the rms electric field of the BBR at $T_0 = 300\,\mathrm{K}$, T_{F} is the average temperature in the free-evolution zone, and $\epsilon = 0.013 \pm 0.001$ is a numerical coefficient evaluated in [38]. At METAS, the FoCS-2 primary standard is located in a temperature-controlled laboratory with the temperature maintained at 295.30 K with annual peak-to-peak variations on the order of 0.15 K (figure 14). The temperature of the interaction zone is actively stabilized with eight heating rods at 296.83 K, where the Ramsey cavity is in resonance with the 9.192 GHz clock frequency. Five NTC sensors located on the aluminium vacuum enclosure monitor fluctuations. These sensors provide a temperature measurement uncertainty of ±0.097 K and we record a difference of 0.15 K between the top and the bottom of the interaction zone. The relative BBR shift for FoCS-2 and the associated uncertainty are calculated to be:

$$\frac{\Delta\nu_{\mathrm{BBR}}}{\nu_0} = (-16.67 \pm 0.04) \times 10^{-15}.$$

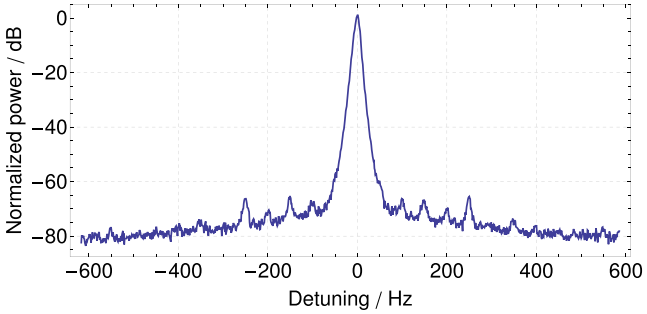

Figure 15. Spectrum of the microwave signal at the output of the microwave synthesizer. The maximum is normalized to 0 dB and chosen to be the central frequency. It corresponds to the 9.192 631 770 GHz signal at the output of the microwave synthesizer measured before the power divider at the top of FoCS-2.

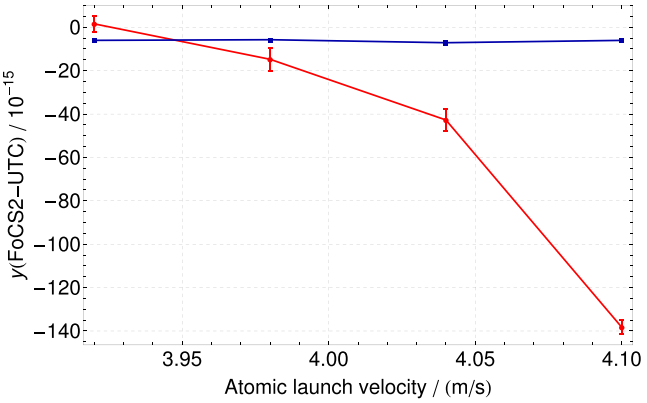

Figure 16. Evolution of the relative frequency y(FoCS-2-UTC) as a function of the launch velocity of the atomic beam. The red curve (dots) shows a variation of 140×10^{-15}. The blue curve (squares) corresponds to the same measurement after the installation of the graphite cylinder. The frequency dependence is then negligible and lies within the measurement uncertainty.

4.4. Microwave effects

Several frequency shifts are due to microwave field perturbations either in the free-evolution region or in the Ramsey cavity. These contributions come from spurious spectral lines in the microwave field spectrum [39], microwave leakage [40], the distributed cavity phase shift (DCPS) [41, 42], microwave lensing [43, 44] and, in the case of the continuous fountain, the end-to-end phase shift [29]. In the following we discuss the microwave spectrum, microwave leakage, the end-to-end phase shift, and the DCPS.

4.4.1. Microwave spectral purity. The commercial microwave synthesizer used to generate the microwave signal to operate FoCS-2 is described in section 2.4. Figure 15 shows the spectrum of the interrogation microwave signal just before it is split and distributed between the two coaxial cables of the Ramsey cavity. As demonstrated in [45] and [39], spurs in the microwave spectrum can lead to a frequency shift. We see in figure 15 no spurs above −65 dBc over a frequency span of 1200 Hz. Following [39] and measurements realized over a larger span (not shown here), we conclude that no frequency shift caused by spurious frequencies on the spectrum

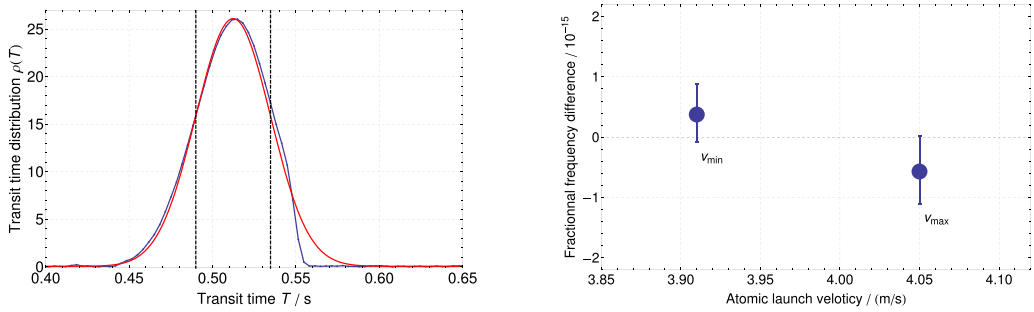

Figure 17. (a) shows the measured transit time distribution for the average transit time of 0.51 s of the atomic beam. This distribution is used to define $T_{min} = 0.49$ s and $T_{max} = 0.53$ s, which correspond to $T_{opt} \pm \sigma$. The two vertical dashed lines show the positions of T_{min} and T_{max}. The blue curve is the measurements and the red curve corresponds to a fit. The difference between these two curves of around $T = 0.56$ s is due to the microwave cavity's velocity selection and cutting of the slowest atomic trajectories. (b) shows the fractional frequency differences $y(\Delta v_{max}) = y(v_{max}) - y(v_{opt})$ and $y(\Delta v_{min}) = y(v_{min}) - y(v_{opt})$.

is greater than 4.48×10^{-17}, which yields an estimate of the relative frequency offset of the fountain of:

$$\frac{\Delta\nu_{spect}}{\nu_0} = (0.00 \pm 0.05) \times 10^{-15}.$$

In the case of our synthesizer, a spur located at +7 MHz (9.2 GHz) of the resonance is observed (+1.5 dB). However it is reduced by 20 dB by the microwave cavity transfer function and thus does not contribute to the frequency shift in a significant way ($\frac{\Delta\nu}{\nu_0} < 1 \times 10^{-17}$).

4.4.2. Microwave current effects and microwave leakage. Due to the continuous operation of the fountain, the microwave signal cannot be turned off during the free flight of the atoms between the two Ramsey interactions. Great care was taken to avoid microwave leakage in the design of the microwave cavity. As described in section 2.3, cutoffs were provided on each side of the two passages of the cavity. Measurements of the microwave field near the cavity before it was installed in FoCS-2 showed no microwave signal leakage above −180 dBm at the nominal operating power. Similar measurements were made after the Ramsey cavity was installed in FoCS-2, showing a residual microwave field with an amplitude ranging from −180 dBm to −150 dBm depending on the position of the RF detector in the free-flight chamber.

In order to quantify the leakages we decided to measure the clock frequency for different atomic launching velocities. The results (the red curve in figure 16) showed a significant relative frequency dependence of 140×10^{-15} when the atomic velocity was varied between 3.92 m s^{-1} and 4.10 m s^{-1}. Analysis showed that this dependence was due to the change of the apogee height of the atomic beam in the presence of a spurious electromagnetic field. When atoms were launched at 4.10 m s^{-1}, the apogee was very close (1 cm) to the two coaxial cables used for feeding the microwave cavity and we observed a significant frequency shift. Several tests according to electromagnetic compatibility domain best practice [46] suggested a microwave current propagated on the outer surface of the coaxial cables.

To solve this problem we shielded the atoms from spurious microwave by painting the coaxial cables with graphite and by protecting the atomic beam above the cavity by installing a graphite cylinder between the coaxial cables and the atoms (see figure 2). This cylinder is located above the Ramsey cavity (close to the two top cutoffs). It is a hollow cylinder whose top end is closed, to attenuate stray electromagnetic fields in the vicinity of the atomic beam in the free-flight chamber. In addition to the graphite cylinder, small graphite disks were placed on the bottom of the free-flight chamber in order to damp any background microwave radiation in the free-flight chamber.

The blue curve (square dots) in figure 16 shows the clock frequency as a function of the atomic launch velocity after these modifications. An almost total cancellation of the velocity dependence was observed, with the frequency difference between the minimum and maximum velocities changing significantly below the noise floor of the measurement ($\sim 0.5 \times 10^{-15}$).

In order to quantify this effect, we used the transit time distribution [47] (figure 17(a)) for the optimal average velocity v_{opt} of 3.98 m s^{-1} and defined two transit times: $T_{max} = T_{opt} + \sigma$ and $T_{min} = T_{opt} - \sigma$, with 2σ being the FWHM. Using T_{min} and T_{max}, we calculated $v_{min} = 3.91$ m s^{-1} and $v_{max} = 4.05$ m s^{-1}. Figure 17(b) shows the fractional frequency differences $y(\Delta v_{max}) = y(v_{max}) - y(v_{opt})$ and $y(\Delta v_{min}) = y(v_{min}) - y(v_{opt})$. This graph gives the residual frequency–velocity dependence at 1σ, which may result from any remaining microwave leakage. We finally calculate $[y(\Delta v_{max}) - y(\Delta v_{min})]/2 = 0.47 \times 10^{-15}$ as an uncertainty on the microwave leaks.

In order to confirm such cancellation, we performed measurements of the atomic transition probability when a strong pulse of microwave was applied in the Ramsey cavity. The principle consists in measuring the atomic transition probability for 1 s, the time required for atoms to go from the 2*D*-MOT to the detection beam. During this second, a short pulse of microwave of 100 ms was applied. This way it was possible to probe the entire atomic trajectory and observe where atoms interacted with the microwave to perform the $|3,0\rangle \rightarrow |4,0\rangle$ transition. Note that the typical power of the injected microwave pulse is equal to +22.5 dBm which is +30 dB higher than the one used in nominal conditions. Figure 18 shows the results of measurements performed before (a) and after (b)

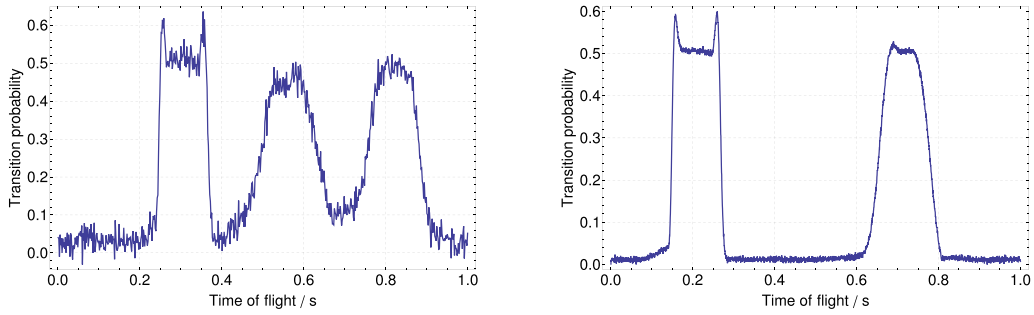

Figure 18. Measurement of the atomic transition probability for 1 s after a short microwave pulse: (a) before the installation of the graphite cylinder; (b) after the graphite cylinder was installed. The vanishing of the peak around 0.5 s in (b) confirms the cancellation of the spurious microwave in the atomic free-precession zone.

the installation of the graphite cylinder. Basically the result expected from these measurements was a flat signal with two peaks originating from the atoms present in the microwave cavity during the 100 ms where the microwave signal was applied. As shown in figure 18(a), a third peak around 0.5 s is visible and is due to the interaction of the atoms with an unwanted source of microwave signal between the two Ramsey interaction zones, thus confirming the hypothesis of a microwave leakage. Figure 18(b) shows the same measurement performed after the installation of the graphite cylinder. The peak at 0.5 s has disappeared even though the measurement was performed at a microwave power level 30 dB higher than the nominal value, thus confirming the efficiency of the graphite cylinder.

4.4.3. End-to-end phase shift. As mentioned in section 2, the microwave cavity has two distinct interaction zones and therefore any geometrical asymmetry between them will produce an end-to-end phase shift. This phase shift $\Delta\phi = \phi_2 - \phi_1$, where $\phi_{1/2}$ is the average phase in the first/second interaction zone, introduces a frequency bias of $\Delta\nu_\phi = -\Delta\phi/(2\pi T)$ [29]. In order to evaluate this shift, we used the cavity reversal mechanism to exchange the two interaction zones with a 180° rotation of the cavity around the vertical axis. By construction, the rotation can be done manually without breaking the vacuum and takes only a few seconds to perform.

To evaluate $\Delta\nu_\phi$, we successively compared the frequencies of FoCS-2 in positions A (original position 0°) and B (rotated by 180°) with the METAS hydrogen maser for 12 h. The frequency shift is then given by $(y\,(\text{position A}) - y(\text{position B}))/2$. The frequency measurements were performed for 6 d and the frequency difference was used to remove the frequency drift of the maser. After averaging of the frequency differences, the frequency shift due to the cavity end-to-end phase shift and the associated uncertainty are:

$$\frac{\Delta\nu_\phi}{\nu_0} = (2.17 \pm 0.27) \times 10^{-15}.$$

4.4.4. Distributed cavity phase shift. In contrast to the end-to-end frequency shift, the DCPS is related to phase variations inside the interaction zones. This effect has been studied in detail in several articles [23, 41, 48, 49]. Due to the continuous working principle of FoCS-2 and its unique cavity design, the evaluation of this effect requires different methods. In this section we describe the methods used to evaluate this effect and the results obtained.

Phase variations or phase gradients of the microwave signal used to realize Ramsey interrogation have different origins. They might come from geometrical (shape, edges, etc) or electrical (conductivity) properties of the cavity and from imperfections in the balance between the two feeding ports. Evaluation is divided into three parts, each corresponding to an internal cavity dimension:

(i) The longitudinal phase gradients along the vertical axis $0z$.
(ii) The transverse parallel phase gradients along the horizontal axis $0x$, which is also the direction of the atomic beam.
(iii) The transverse perpendicular phase gradients along the horizontal axis $0y$, which is perpendicular to the atomic beam plane.

We propose three different methods to evaluate independently each of these contributions. The longitudinal gradients, which depend on the geometry of the cavity, the number of feeding ports and the wall resistivity, are studied by measuring the clock frequency at different microwave power levels. The transverse parallel gradients, which depend on the resistivity of the walls of the cavity and on their geometries, are studied by measuring the clock frequency after a modification of the detected atomic beam shape. In this direction, the modification is made by blocking a part of the detection beam. In a similar way, the transverse perpendicular gradients, which essentially depend on the balance between the two feeding ports of the cavity, are studied by measuring the clock frequency after geometrical modification of the atomic beam. Here, the modification is made by blocking a part of the atomic beam with a graphite plate just before detection. These two methods are illustrated in figures 19(a) and (b). They allow the selection of the two halves of the atomic beam in the two horizontal directions $0x$ and $0y$. The efficiency of these geometrical selections was verified numerically using Monte Carlo simulations and is illustrated in figure 20.

The results obtained with these evaluation methods are also compared with those of numerical simulations based on

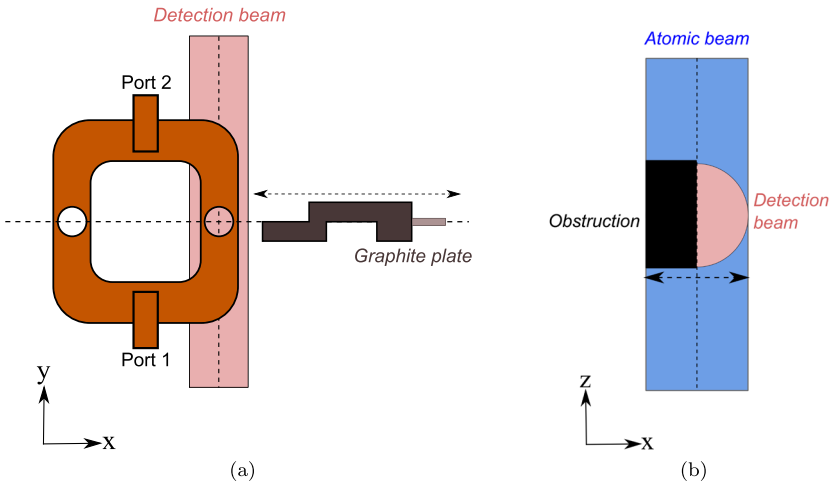

Figure 19. (a) shows the method used to modify the atomic beam shape. It is a top view of the microwave cavity. A graphite plate is placed on the atomic beam trajectory, below the cavity, a few centimetres above the detection beam. This graphite plate is mounted on a linear translation stage, controllable from the outside of the vacuum chamber. Its particular shape allows us to select the front half or the back half of the atomic beam along the $0y$ axis. (b) shows a side view of the atomic beam in the region of detection. The blue rectangle represents the atomic beam while the red circle represents the detection beam. A rectangular graphite plate is placed in the detection beam before it enters the vacuum chamber, to modify its shape and thus limit the detected atoms with about half going through either of the $0x$ axis halves of the cavity interaction zones. This way, we can measure the clock frequency with the left half or the right half of the atomic beam (modification along the $0x$ axis).

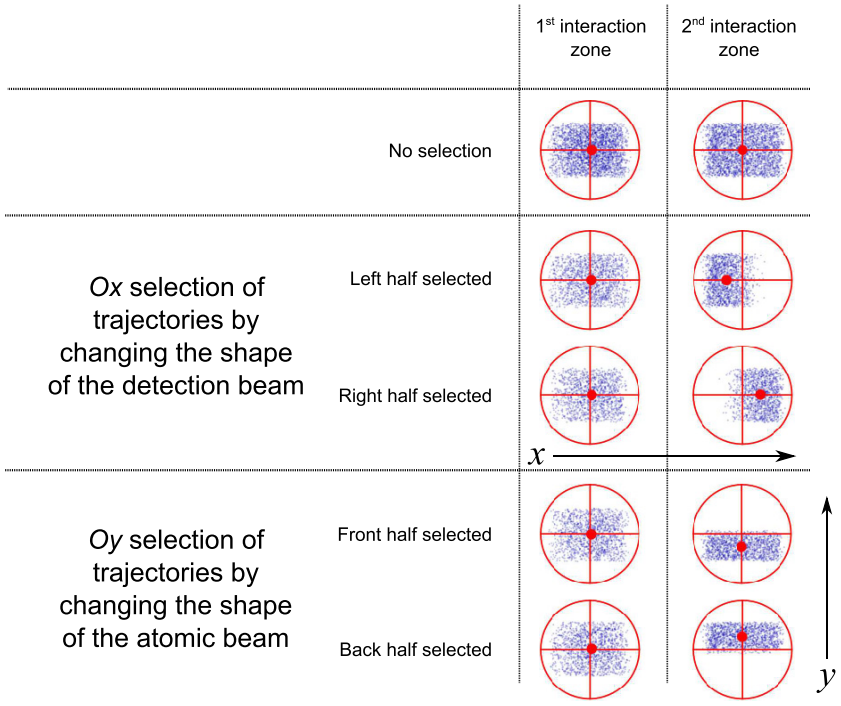

Figure 20. Illustration of the geometrical selection made on the atomic beam. The blue points represent the atoms that reach the detection beam. For any configuration, the first interaction zone is always entirely probed by the atoms. For the left/right selections ($0x$ axis) the centre of mass of the atomic beam is shifted by ± 2 mm while it is shifted by ± 1.25 mm for the front/back selections ($0y$ axis). The rectangular shape of the atomic beam is due to the diaphragms placed on the four cutoffs. They prevent atoms from getting too close to the borders of the cavity holes (represented by the red circles), where phase gradients are known to be potentially large.

the Monte Carlo method. These simulations use the microwave field distribution modelled by the finite-element method (FEM) and are presented in section 2.3 to estimate the effect of the phase gradients on the clock frequency.

In the following, these evaluation methods, in addition with Monte Carlo simulation, are used to determine the maximum value of the frequency shift induced by the DCPS. This value value does not deliver the absolute frequency bias but gives a good estimate of the worst-case frequency deviation, which will be interpreted as the worst-case uncertainty.

Longitudinal phase gradients. Longitudinal phase gradients occur along the vertical axis $0z$. Depending on the geometry of the cavity and on the number of feeding ports, their effect

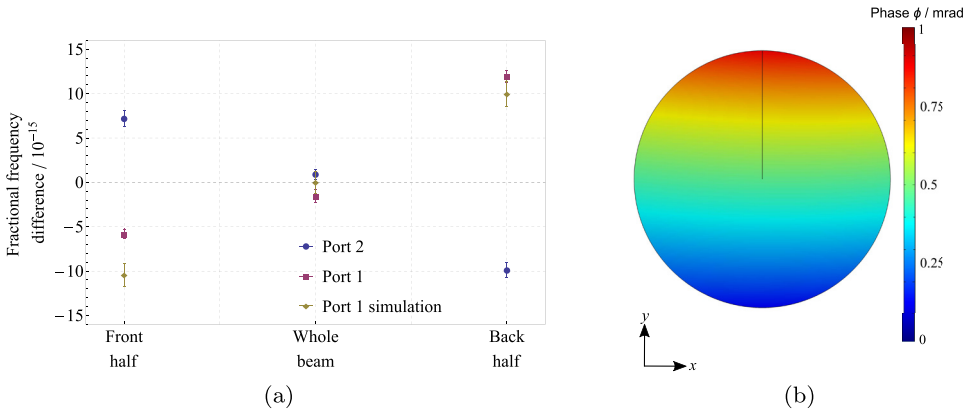

Figure 21. (a) shows the fractional frequency difference of the clock for different positions of the graphite plate. Each point is the difference between the clock frequencies when only one port is used (asymmetrical feeding) and when the two ports are used (symmetrical feeding). The yellow points are based on Monte Carlo simulations, when only port 1 is used to feed the cavity. Note that the simulation with port 2 is not presented, but it shows the same behaviour with an opposite sign. (b) shows the modelled normalized phase variation in the first interaction zone when only port 1 is used. The phase decreases linearly along the y axis. The phase variation when port 2 is used is not presented here, but it shows the same slope with an opposite sign.

on the clock frequency varies with the microwave power during the Ramsey interrogation. In MOT-based fountains and in pulsed fountains, the size of the cloud of cold atoms is different between the upward and downward parts of the trajectory. Hence, the longitudinal phase gradients are not cancelled [23]. The situation is different in FoCS-2, as the source of the atomic beam is a moving molasses which has a diameter larger than the cutoff apertures ensuring that the whole surface of the interaction zones is filled with atoms. As a consequence, the frequency shift induced by the longitudinal phase gradients should be, at most, in the same order of magnitude as that observed in pulsed fountains. In both pulsed and continuous fountains, the frequency shift can be evaluated by measuring the clock frequency at different values of the microwave power [50]. Several precautions should be taken for this kind of measurement to be valuable since other effects, such as microwave leakages and the collisional shift, may also modify the clock frequency when the microwave power is changed [51].

In order to give an upper limit to this frequency shift we measured the clock frequency for $\pi/2$ and $3\pi/2$ pulses alternately. In these two cases we supposed that there were no microwave leakages and we neglected the difference of -3×10^{-17} on the frequency clock induced by the collisional shift which was obtained from the variation of the atomic signal by using the method described in section 4.5. Each measurement lasted 4 h and after 120 repetitions we obtained an average difference between the clock frequencies at $\pi/2$ and $3\pi/2$ of $(0.084 \pm 4.440) \times 10^{-16}$. We take the uncertainty of this difference as the uncertainty of the frequency shift induced by the longitudinal phase gradients.

Transverse parallel phase gradients. In the TE_{105} microwave cavity of FoCS-2, the transverse parallel phase gradients are mostly due to the resistivity of the walls of the cavity [23, 29]. In pulsed fountains [1, 2, 4, 49], the frequency shift due to this effect is partly evaluated by tilting the fountain in order to probe several parts of the interaction zone. As the atomic beam in FoCS-2 is wider than the rectangular diaphragms limiting the size of the interaction zones, tilting the fountain is not useful for evaluating these phase gradients. Instead, we select atomic trajectories covering only one half of the second interaction zone as illustrated in figures 19(a) (0x) and 19(b) (0y).

In this case of transverse parallel phase gradients, geometrical selection is performed along the 0x axis. As with the longitudinal phase gradients, we alternated measurements of the clock frequency where the left or the right half of the beam was selected. The average frequency difference given by these measurements is $(0.18 \pm 0.51) \times 10^{-15}$. Monte Carlo simulations realized in the same conditions give a frequency difference of $(0.54 \pm 0.20) \times 10^{-15}$. These results are compatible with the measurements within the estimated measurement uncertainties. We thus decided to take the uncertainty of the difference as the uncertainty of the frequency shift induced by transverse parallel phase gradients.

Transverse perpendicular phase gradients. In this direction, the phase gradients are due to the non-zero resistivity of the cavity walls combined with an imbalance of the microwave power in the two feeding ports. For the same reasons as discussed before, we performed a geometrical selection of the atomic beam. As the phase gradients to be evaluated were along the 0y axis, it was not possible to realize geometrical selection with the detection beam. Consequently, as shown in figure 19(a) and described above, a graphite plate was installed in the vacuum chamber in order to block a part of the atomic beam. Hence we performed measurements of the clock frequency with the front half and the back half of the atomic beam. In addition, as in this case the phase gradients depended on the balance between the two feeding ports, we measured the clock frequency by only using one feeding port in order to amplify the phase gradient variation. The balance between the feeding ports was controlled by a phase shifter and a variable attenuator placed at the top of the fountain.

The results of these measurements are shown in figure 21(a). Each point is the fractional frequency difference between the clock frequencies when one port (1 or 2) is used (asymmetrical feeding) and when the two ports are used (symmetrical feeding). This way, the result is not affected

Table 2. Summary of the different contributions of the DCPS frequency shift.

Physical effect	Shift (10^{-15})	Uncertainty (10^{-15})
Longitudinal gradients	—	0.44
Transverse parallel gradients	—	0.51
Transverse perpendicular gradients	—	0.77
Total DCPS	—	1.03

by the maser drift. Results show that the clock frequency variation is 18.1×10^{-15} between the case where the front half is selected and the case where the back half is selected. Following figure 20, this geometrical selection induces an offset of the centre of mass of the atomic beam of 1.25 mm. From figure 21(a), we obtain a linear dependency of the clock frequency as a function of the position of the centre of mass of the atomic beam of $7.7 \times 10^{-15}\text{mm}^{-1}$ when only port 1 is used.

This measurement does not give the frequency dependence when the fountain is in the nominal regime. As we only get the frequency difference in absolute terms, the frequency dependence with a symmetrical feeding can be higher than the one presented here. However, in agreement with the simulations presented in section 2.3 and in figure 21(b), the clock frequency dependence in the asymmetrical case is also linear and the sign of the slope changes with the choice of feeding port. As can be observed in figure 21(a), the same is true for the frequency difference dependence. This way, the clock frequency dependence in the symmetrical case cannot exceed $7.7 \times 10^{-15}\text{mm}^{-1}$.

Taking this into account and assuming that in the nominal regime the centre of mass of the atomic beam has an uncertainty of 0.1 mm (thanks to the orientable platform base), we take the worst possible case of a totally unbalanced feeding of the cavity to determine a frequency uncertainty of 0.77×10^{-15} for the effect of transverse perpendicular phase gradients.

Summary of the results and conclusion. Table 2 summarizes the results presented above. The total uncertainty of the frequency shift induced by the DCPS is 1.03×10^{-15}. We demonstrate that the evaluation methods described in this section are sufficient to give a realistic upper limit to the effect. They are also a first step to a further, more precise evaluation of the DCPS frequency shift.

4.5. Collisional shift

In a continuous beam fountain, the low density of the atomic beam (10^5 atoms cm^{-3}) and its high longitudinal temperature (80 μK) reduce the frequency shift due to collisions between Cs atoms during their interrogation [11].

In order to evaluate this effect, frequency measurements were made for different atomic densities [52, 53]. The intensity of the repumping beam of the 2D-MOT was varied to change the 2D-MOT cooling efficiency and thus the atomic beam density in the fountain beam. Under normal operating conditions, FoCS-2 works with its highest density. Therefore series of measurements were made with different, lower atomic densities. The results are shown in figure 22. Each point is the fractional frequency difference between a given atomic density and the optimal atomic density. In this way the frequency drift of the maser is cancelled. The size of the error bars depends on the measurement time of a few hours to a few days. Using linear regression and assuming zero shift at zero density, we estimate that the collisional shift and its statistical uncertainty are:

$$\frac{\Delta\nu_C}{\nu_0} = (-1.91 \pm 1.47) \times 10^{-15}.$$

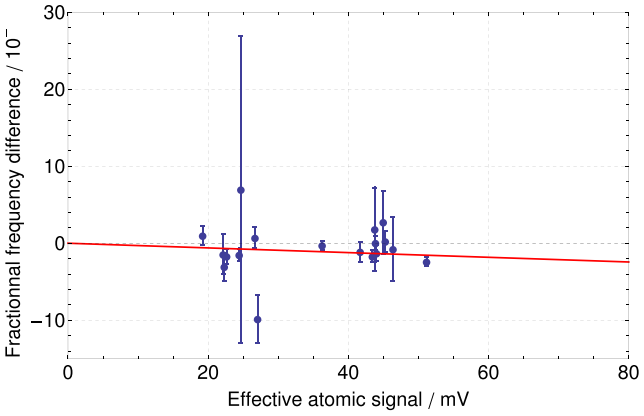

Figure 22. Fractional frequency difference as a function of the effective atomic signal which is proportional to the atomic density. This measurement allows the evaluation of the frequency shift due to collisions.

4.6. Light shifts

As mentioned in section 3, the lasers used to prepare and to detect the continuous atomic beam are always active and therefore light scattered from the source and the detection regions may produce a light shift of the clock transition, which has to be evaluated. The light shift produced by the fluorescence originating from the source chamber and the light shift produced by the fluorescence originating from the detection zone are treated separately.

4.6.1. Light shift due to the source light. Prior to the installation of the light trap, the clock frequency was measured as a function of the light power coming from the source chamber. The light power was measured with a photodiode located 5 cm above the ESM location and the FoCS-2 frequency with respect to UTC via the hydrogen maser. In order to vary the intensity of the fluorescence, the power of the 2D-MOT laser was reduced (result shown in figure 23). Before the light trap was installed, the light intensity reaching the photodiode when the fountain was at the nominal flux was 4.3 ± 0.2 nW cm^{-2}. This intensity induced a frequency shift of $\Delta\nu_{\text{LS}}^{\text{before}} = -1.6 \times 10^{-12}$. After installation of the light trap, the light intensity reaching the photodiode was $I^{\text{after}} = 433 \pm 100$ fW cm^{-2}, which was

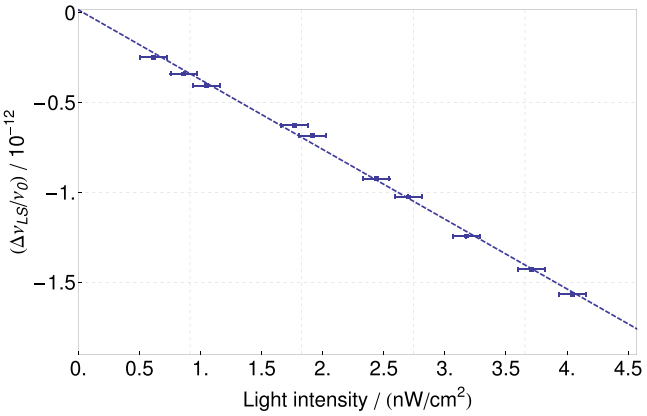

Figure 23. Fractional frequency shift measured on FoCS-2 before installation of the light trap as a function of the light intensity measured on the photodetector placed in the vicinity of the light trap.

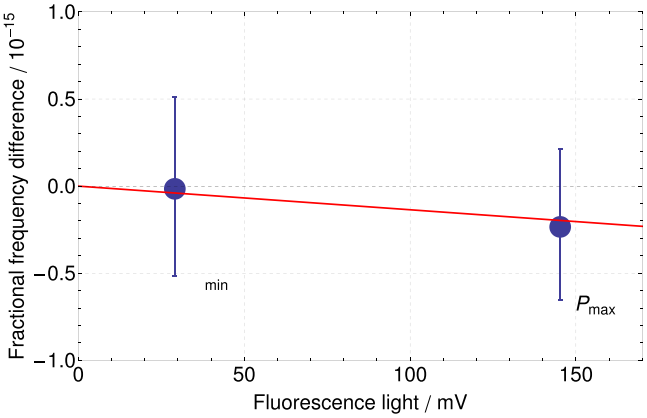

Figure 24. Fractional frequency difference as a function of the fluorescence intensity. This measurement allows us to evaluate the frequency shift due to light in the detection chamber.

attenuated by a factor of 10^4. Therefore the light shift with the light trap and the associated uncertainty are:

$$\frac{\Delta\nu_{\mathrm{LS}}}{\nu_0} = (-0.16 \pm 0.04) \times 10^{-15}.$$

4.6.2. Light shift due to the detection light. As described in section 2, there is presently no light trap to protect the atoms from the light coming from the detection region. In order to evaluate the frequency shift due to this effect, measurements were made with different intensities of the probe beam. Each series consisted of repeated sequences of four measurements of 1800 s with four power values: $P_{\mathrm{min}} \to P_{\mathrm{opt}} \to P_{\mathrm{max}} \to P_{\mathrm{opt}}$ where P_{opt} is the probe power when FoCS-2 is in the optimal working regime, $P_{\mathrm{min}} = P_{\mathrm{opt}}/2$ and $P_{\mathrm{max}} = 2P_{\mathrm{opt}}$. Figure 24 shows the results of the measurements. By using linear regression and assuming zero shift at zero power we estimate that the detection light shift and its uncertainty are:

$$\frac{\Delta\nu_{\mathrm{LD}}}{\nu_0} = (-0.10 \pm 0.41) \times 10^{-15}.$$

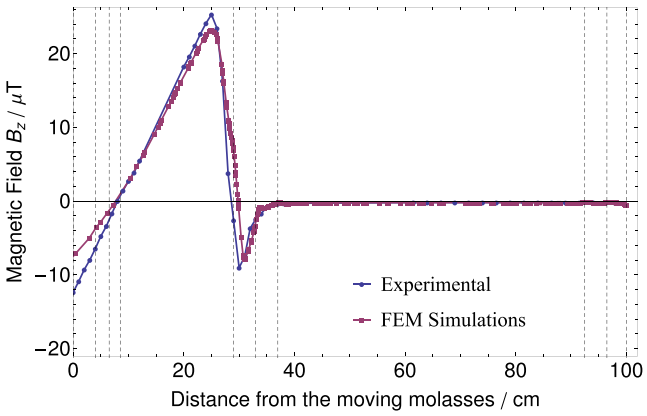

Figure 25. Comparison between the measurements and the results of our finite-element simulations of the vertical component of the magnetic field along FoCS-2. The vertical dashed lines represent from left to right the first optical lattice, the second optical lattice, the depumping beam, the three lower magnetic shield plates and the three upper magnetic shield plates. This comparison was made before the corrections presented in figure 26.

4.7. Cavity pulling

The cavity pulling frequency shift comes from an offset of the cavity resonance frequency with respect to the atomic transition frequency. This effect, described in [29], can be calculated using:

$$\frac{\Delta\nu_{\mathrm{CP}}}{\nu_0} = \frac{\Delta f}{\nu_0} \times \frac{8}{\pi^2} \left(\frac{Q_{\mathrm{C}}}{Q_{\mathrm{at}}}\right)^2 \times b\tau \cot(b\tau), \qquad (4)$$

where Δf is the detuning of the Ramsey cavity, τ the average interaction time of an atom in the Ramsey cavity, Q_{at} the atomic quality factor, Q_{C} the loaded quality factor introduced in section 2.3 and b the Rabi circular frequency of the clock transition. Given the actual temperature stability of the vacuum chamber and the cavity, the detuning is less than 15 kHz. The interrogating pulse is within 20% of the optimum $\pi/2$ pulse. Therefore the frequency shift and the associated uncertainty are:

$$\frac{\Delta\nu_{\mathrm{CP}}}{\nu_0} = (0.000 \pm 0.003) \times 10^{-15}.$$

4.8. Majorana transitions

Majorana transitions occur when atoms pass through a region of zero magnetic field or a region that shows strong variations of the amplitude of the magnetic field that do not satisfy the adiabatic condition [1, 54–56]. In PFSs, Majorana transitions may induce coherences between the Zeeman sublevels. These $\Delta F = 0$, $\Delta m_F = \pm 1$ atomic transitions can occur between the state selection and the first Ramsey interrogation, and after the second Ramsey interrogation, and cause a frequency shift.

Due to technical limitations, it is very difficult to measure the full 3D magnetic field along the atomic trajectory. The alternative is to use FEMs to simulate the magnetic field distribution. In order to confirm these simulations, simulations and

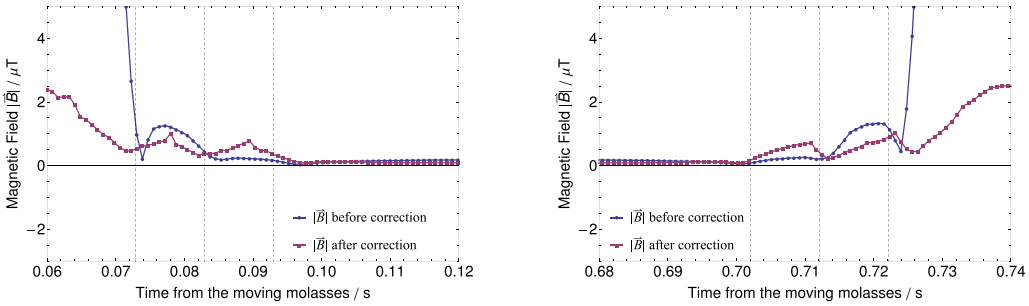

Figure 26. Behaviour of the vector norm of the magnetic field along the parabolic trajectory before (blue line) and after (red line) the adjustment of the triplet of coils. Figures (a) and (b) show the comparison for, respectively, the upward and downward parts of the atomic trajectory. The vertical dashed lines represent the magnetic shield plates. Between 0.12 s and 0.68 s, the magnetic field is constant.

Table 3. Uncertainty budget of FoCS-2. The splitting into type-A and type-B evaluation aims to classify quantities into those whose uncertainties are limited by either type-A or type-B evaluations.

Physical effect	Shift (10^{-15})	Uncertainty (10^{-15})
Type-B evaluation		
Second-order Zeeman	23.59	0.21
Gravitational	59.72	0.02
Second-order Doppler	−0.01	<0.01
Blackbody radiation	−16.67	0.04
Microwave spectrum purity	0.00	0.05
Light shift source	−0.16	0.04
Cavity pulling	0.00	<0.01
Rabi pulling	0.00	0.02
Ramsey pulling	0.05	0.10
Type-A evaluation		
End-to-end	2.17	0.27
Collisional Cs–Cs	−1.91	1.47
Light shift detection	−0.10	0.41
RF leakage	0.00	0.47
Majorana transitions	0.00	0.50
DCPS	—	1.03
Total	66.68	1.99

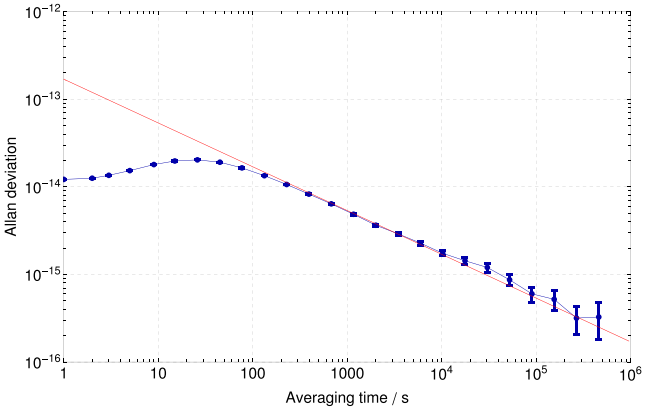

Figure 27. Relative Allan deviation of the frequency difference between FoCS-2 and the METAS hydrogen maser ID 1405701 for 30 d of measurement. The short-term stability at 1 s is 1.7×10^{-13} for this measurement.

measurements of the vertical component of the magnetic field realized with a fluxgate magnetometer along a vertical axis in FoCS-2 were compared. This comparison, shown in figure 25, demonstrates excellent agreement between the FEM simulations and the measurements and validates the simulations.

As described in section 2.1, FoCS-2 has two triplets of coils for adjusting the magnetic field. These triplets were modelled in the FEM simulation to modify the behaviour of the magnetic field in order to remove all zero crossing points. Figure 26 shows simulations of the magnetic field amplitude $|\vec{B}|$ along the atomic trajectory before and after modifications of the current in the triplet of coils. The two figures show the behaviour of the magnetic field in the vicinity of the external layer of the magnetic shield. Even if there were no zero crossing points to remove between the previous and new magnetic configurations, the new parameters decrease the rate of variation of $|\vec{B}|$. Note that in these two cases the magnetic field in the free-flight chamber is homogeneous and constant.

In order to study a frequency shift due to a Majorana transition as described in [56], the magnetic field in FoCS-2 was modified to generate regions where the adiabatic condition was not satisfied. These measurements show no evidence of a frequency shift in the limits of their statistical uncertainties. Based on this analysis and on the different measurements that were made, we estimate that the frequency shift due to Majorana transitions in FoCS-2 is zero within the measurement uncertainty:

$$\frac{\Delta\nu_{\mathrm{Maj}}}{\nu_0} = (0.00 \pm 0.50) \times 10^{-15}.$$

4.9. Rabi and Ramsey pulling

Rabi pulling is related to $\Delta F = \pm 1, \Delta m_F = 0$ atomic transitions (π-transitions) while Ramsey pulling describes $\Delta F = \pm 1, \Delta m_F = \pm 1$ atomic transitions (σ-transitions). Even if these two effects lead to smaller frequency shifts in fountain clocks than in thermal beam clocks, the state preparation of FoCS-2 requires a close examination of these effects.

The frequency shift due to Rabi pulling is explained by asymmetric populations on the Zeeman sublevels $m = \pm 1$. The following formula [57] allows the calculation of the Rabi

Table 4. Measurements of TAI realized with FoCS-2. The values are expressed in units of 10^{-15}.

Measurement period	u_A	u_B	u_{lab}	u_{TAI}	u	d(FoCS-2-TAI)	d(CircT)	Δd
57 809–57 839	0.11	1.99	0.07	0.20	2.00	-0.78 ± 2.00	-0.75 ± 0.22	-0.03 ± 2.02
57 919–57 934	0.20	1.99	0.07	0.53	2.07	-0.23 ± 2.07	0.09 ± 0.22	-0.32 ± 2.08
57 944–57 964	0.17	1.99	0.07	0.30	2.02	-0.11 ± 2.02	0.07 ± 0.26	-0.17 ± 2.04

frequency shift for an optimal $\pi/2$ pulse at $m = 0$ for a monokinetic beam:

$$\frac{\Delta\nu_{\mathrm{Rab}}}{\nu_0} \cong \frac{S_{-1} - S_{+1}}{S_0} \times \frac{\tau}{T} \times \frac{15\pi^5 \left(4\epsilon\tau(1+\cos(\epsilon\tau)) + ((\epsilon\tau)^2 - \pi^2)\sin(\epsilon\tau)\right)}{256\,\nu_0 T\,((\epsilon\tau)^2 - \pi^2)^3}. \tag{5}$$

Here S_{-1}, S_{+1} and S_0 are, respectively, the atomic population on the Zeeman sublevels $|F = 3, m_F = -1\rangle$, $|F = 3, m_F = +1\rangle$ and $|F = 3, m_F = 0\rangle$. τ is the transit time of an atom in the Ramsey cavity, T is the time between the two Ramsey interactions and $\epsilon = 4\pi \times f_z$ where $f_z = 240$ Hz is the Zeeman frequency. In FoCS-2, $\frac{S_{-1}-S_{+1}}{S_0} = 7\%$, $\tau = 8$ ms and $T = 0.51$ s, which leads to a frequency shift below 10^{-17} and a type-B uncertainty of 1.6×10^{-17}. Note that in FoCS-2 the relatively large atomic velocity distribution will further reduce the frequency shift.

The frequency shift due to Ramsey pulling is due to a non-zero angle between the C-field and the microwave field inside the Ramsey cavity. The finite-element simulations described in section 4.8 were used to evaluate this angle when FoCS-2 is under normal operating conditions. This angle, averaged on thes typical atomic beam trajectory, is 0.3°. According to [58], the frequency shift due to Ramsey pulling can be calculated as:

$$\frac{\Delta\nu_{\mathrm{Ram}}}{\nu_0} = -\frac{\sqrt{3}}{2\,\nu_0 T}\frac{b\sin(\theta)}{\epsilon\sin(b\tau)} \times c, \tag{6}$$

where b is the Rabi frequency, θ is the angle between the C-field and the RF field, c is the ground-state coherence value and $\epsilon = 4\pi \times f_z$ where $f_z = 240$ Hz is the Zeeman frequency. In order to evaluate the value of c measurements were performed with different values of the angle θ. This angle can be modified by injecting a current in a copper wire located in the free-flight chamber and usually used to demagnetize the magnetic shields. These measurements and the finite-element simulations allow us to estimate the value of the ground-state coherence as -0.0014 ± 0.0001. Based on this analysis, we evaluate the frequency shift and the related uncertainty as:

$$\frac{\Delta\nu_{\mathrm{Ram}}}{\nu_0} = (0.05 \pm 0.10) \times 10^{-15}.$$

5. Results of the FoCS-2 accuracy evaluation

Table 3 summarizes the frequency shifts and their uncertainties for all the effects discussed in section 4. The uncertainty budget is strongly dominated by the collisional Cs–Cs shift and the DCPS whose uncertainties are statistical and are obtained from measurements averaged over 10 d. The total uncertainty coming from type-A evaluation (dominated by collisions) is 1.98×10^{-15} and the total uncertainty coming from type-B evaluation (dominated by the second-order Zeeman) is 0.22×10^{-15}. Therefore the total uncertainty of FoCS-2 is 1.99×10^{-15}.

6. Comparison with TAI

Following the evaluation of the accuracy budget of the fountain, frequency comparisons of FoCS-2 to TAI were performed. The two-way satellite link [59] comparison technique was used to realize these measurements. The METAS hydrogen maser (ID 1405701) used to realize UTCH(CH) was also used as a local oscillator for FoCS-2.

Three measurements were made. All these measurements were made without any dead time. The first one was performed for 30 d and the two others were carried out over 20 d. Figure 27 shows the Allan deviation of the full-month comparison made in March 2017. It has a deviation of $\sigma_y(\tau) = 1.7 \times 10^{-13}\ \tau^{-1/2}$.

The comparison was performed by estimating the d value of FoCS-2, d(FoCS-2-TAI), and its uncertainty u and by comparing them with those reported by the BIPM in *Circular T*. The uncertainty u is the quadratic sum of four contributions: u_A, the uncertainty originating in the instability of the standard; u_B, the combined uncertainty from systematic effects; u_{lab}, the uncertainty in the link between the standard and the clock participating in TAI; and finally, u_{TAI}, the uncertainty in the link to TAI. The results of the comparisons between FoCS-2 and TAI are presented in table 4. The value of d published by the BIPM during the same period called d(CircT) and Δd which is the difference between the two estimations are also reported.

The three periods of comparison between FoCS-2 and TAI show that the differences $\Delta d = d$(FoCS-2-TAI)$-d$(CircT) all remain smaller than the total uncertainty, whose presently dominating contribution is the uncertainty of FoCS-2.

7. Conclusions

In this paper we present an evaluation of the uncertainty budget of the FoCS-2 PFS located at METAS, the Federal Institute of Metrology in Switzerland. The budget establishes a current uncertainty of 1.99×10^{-15}, strongly dominated by type-A evaluations. This work demonstrates the experimental performance of a continuous fountain and shows the first informal comparisons to TAI. These comparisons show results that are fully compatible with the uncertainty budget and suggest that

the fountain is now sufficiently mature to consider an official contribution to TAI.

The evaluation of FoCS-2 will be further improved by analysing effects like microwave lensing or background collisional shift, which should remain in the 10^{-16} level [4, 49]. The dominating effects at the moment are the collisional shift and the DCPS which both need more extensive evaluations in order to reduce the global uncertainty to below the 10^{-15} level. To achieve this goal, some hardware modifications are already planned, as well as new DCPS measurements using new patterns for the geometrical selection of the atomic beam.

Acknowledgments

This work was supported by the Swiss National Science Foundation. The authors thank Dr Stefan Weyers for the helpful discussions about microwave leakages.

References

[1] Heavner T P, Donley E A, Levi F, Costanzo G, Parker T E, Shirley J H, Ashby N, Barlow S E and Jefferts S R 2014 *Metrologia* **51** 174–82
[2] Guéna J *et al* 2012 *IEEE Trans. Ultrason. Ferroelectr. Freq. Control* **59** 391–410
[3] Szymaniec K, Park S E, Marra G and Chalupczak W 2010 *Metrologia* **47** 363–76
[4] Fang F, Li M, Lin P, Chen W, Liu N, Lin Y, Wang P, Liu K, Suo R and Li T 2015 *Metrologia* **52** 454–68
[5] Gerginov V, Nemitz N, Weyers S, Schröder R, Griebsch D and Wynands R 2010 *Metrologia* **47** 65–79
[6] Domnin Y S, Baryshev V N, Boyko A I, Elkin G A, Novoselov A V, Kopylov L N and Kupalov D S 2013 *Meas. Tech.* **55** 1155–62
[7] Levi F, Calonico D, Calosso C E, Godone A, Micalizio S and Costanzo G A 2014 *Metrologia* **51** 270–84
[8] Berthoud P, Fretel E and Thomann P 1999 *Phys. Rev.* A **60** 4241–4
[9] Di Domenico G 2004 Collimation d'un jet continu d'atomes de césium par refroidissement laser *PhD Thesis* Université de Neuchâtel
[10] Castagna N, Guéna J, Plimmer M D and Thomann P 2006 *Eur. Phys. J. Appl. Phys.* **34** 21–30
[11] Dudle G, Mileti G, Joyet A, Fretel E, Berthoud P and Thomann P 2000 *IEEE Trans. Ultrason. Ferroelectr. Freq. Control* **47** 438–42
[12] Joyet A 2003 Aspects métrologiques d'une fontaine continue à atomes froids *PhD Thesis* Université de Neuchâtel
[13] Di Domenico G, Devenoges L, Joyet A, Stefanov A and Thomann P 2011 Uncertainty evaluation of the continuous cesium fountain frequency standard FOCS-2 *Proc. Joint Conf. of the IEEE Int. Frequency Control and the European Frequency and Time Forum (FCS)* (San Francisco)
[14] Devenoges L 2012 Evaluation métrologique de l'étalon primaire de fréquence à atomes froids de césium FoCS-2 *PhD Thesis* Université de Neuchâtel
[15] Joyet A, Mileti G, Dudle G and Thomann P 2001 *IEEE Trans. Instrum. Meas.* **50** 150–6
[16] Füzesi F, Jornod A, Thomann P, Plimmer M D, Dudle G, Moser R, Sache L and Bleuler H 2007 *Rev. Sci. Instrum.* **78** 103–9
[17] Di Domenico G, Devenoges L, Dumas C and Thomann P 2010 *Phys. Rev.* A **82** 053417
[18] Cohen-Tannoudji C N 1998 *Rev. Mod. Phys.* **70** 707–19
[19] Audoin C, Giordano V, Dimarcq N, Cérez P, Petit P and Théobald G 1994 *IEEE Trans. Ultrason. Ferroelectr. Freq. Control* **43** 515–20
[20] Guérandel S, Hermann V, Barillet R, Cérez P, Théobald G, Audoin C, Chassagne L, Sallot C and Delporte J 2002 Operation of a compact cesium beam tube: how to improve the stability towards the 10-12t-1/2 level *IEEE Int. Frequency Control Symp. and PDA Exhibition (New Orleans)* pp 480–3
[21] Guerandel S, de Clercq E, Barillet R and Audoin C 2007 In-depth analysis of the frequency stability of optically pumped cesium beam frequency standards *IEEE Int. Frequency Control Symp. Joint with 21st European Frequency and Time Forum (Geneva)* pp 1050–5
[22] Li R and Gibble K 2004 *Metrologia* **41** 376–86
[23] Li R and Gibble K 2010 *Metrologia* **47** 534–51
[24] Bernier L G, Dudle G and Schlunegger C 2007 New real time UTC(CH) generation scheme at METAS: recent progress in control and calibration methods *IEEE Int. Frequency Control Symp. Joint with 21st European Frequency and Time Forum* pp 385–90
[25] Bernier L G and Schaller G 2011 A new system for generation of UTC(CH) *Proc. 43rd Annual Precise Time and Time Interval Systems and Applications Meeting (PTTISAM, Long Beach)* pp 153–62
[26] Devenoges L, Di Domenico G, Stefanov A, Jallageas A, Morel J, Südmeyer T and Thomann P 2017 *Metrologia* **54** 239–46
[27] Di Domenico G, Devenoges L, Stefanov A, Joyet A and Thomann P 2011 *Eur. Phys. J. Appl. Phys.* **56** 11001
[28] Petit G and Wolf P 2005 *Metrologia* **42** 138–44
[29] Vanier J and Audoin C 1989 *The Quantum Physics of Atomic Frequency Standards* (Philadelphia: Hilger)
[30] BIPM 2013 Practical realization of the definition of the unit of time *Technical Report* BIPM Paris
[31] Itano W M, Lewis L L and Wineland D J 1982 *Phys. Rev.* A **25** 1233–5
[32] Simon E, Laurent P and Clairon A 1998 *Phys. Rev.* A **57** 436–9
[33] Jefferts S R, Heavner T P, Parker T E, Shirley J H, Donley E A, Ashby N, Levi F, Calonico D and Costanzo G A 2014 *Phys. Rev. Lett.* **112** 050801
[34] Bauch A, Fischer B, Heindorff T and Schröder R 1998 *Metrologia* **35** 829–45
[35] Augustin R, Bauch A and Schröder R 1997 Shift of the caesium hyperfine transition frequency due to blackbody radiation experimental verification and related studies *11th European Frequency and Time Forum (Neuchâtel)* pp 47–52
[36] Robyr J L, Knowles P and Weis A 2014 *Phys. Rev.* A **90** 012505
[37] Rosenbusch P, Zhang S and Clairon A 2007 Blackbody radiation shift in primary frequency standards *Proc. IEEE Int. Frequency Control Symp. and 21st European Frequency and Time Forum (Geneva)* pp 1060–3
[38] Angstmann E J, Dzuba V A and Flambaum V V 2006 *Phys. Rev.* A **74** 023405
[39] Levi F, Shirley J H, Heavner T P, Yu D H and Jefferts S R 2006 *IEEE Trans. Ultrason. Ferroelectr. Freq. Control* **53** 1584–9
[40] Weyers S, Schröder R and Wynands R 2006 Effects of microwave leakage in caesium clocks: theoretical and experimental *Proc. 20th European Frequency and Time Forum (Braunschweig)* pp 173–80
[41] Guéna J, Li R, Gibble K, Bize S and Clairon A 2011 *Phys. Rev. Lett.* **106** 130801

[42] Weyers S, Gerginov V, Nemitz N, Li R and Gibble K 2012 *Metrologia* **49** 82–7
[43] Gibble K 2014 *Phys. Rev.* A **90** 015601
[44] Jefferts S R, Heavner T P, Barlow S E and Ashby N 2015 *Phys. Rev.* A **91** 067601
[45] Audoin C, Jardino M, Cutler L S and Lacey R F 1978 *IEEE Trans. Instrum. Meas.* **27** 325–9
[46] Wilhelm J 1992 *Elektromagnetische Verträglichkeit: (EMV)* (Renningen, Germany: Expert-Verl)
[47] Shirley J H 1997 *IEEE Trans. Instrum. Meas.* **46** 117–21
[48] Jefferts S R, Shirley J H and Ashby N 2005 *IEEE Trans. Ultrason. Ferroelectr. Freq. Control* **52** 2314–21
[49] Li R, Gibble K and Szymaniec K 2011 *Metrologia* **48** 283
[50] Li R and Gibble K 2005 Distributed cavity phase and the associated power dependence *Proc. 2005 IEEE Int. Frequency Control Symp. and Exposition* (IEEE) pp 99–104
[51] Szymaniec K, Chalupczak W, Weyers S and Wynands R 2007 *Appl. Phys.* B **89** 187–93
[52] Sortais Y, Bize S, Nicolas C, Clairon A and Salomon C 2000 *Phys. Rev. Lett.* **85** 3117–20
[53] Szymaniec K, Chałupczak W, Tiesinga E, Williams C J, Weyers S and Wynands R 2007 *Phys. Rev. Lett.* **98** 153002
[54] Majorana E 1932 *Il Nuovo Cimento* **9** 43–50
[55] Bauch A and Heindorff T 1985 Experimental studies on majorana transitions in a Cs atomic beam frequency standard *39th Annual Symp. on Frequency Control* (IEEE) pp 8–12
[56] Wynands R, Schröder R and Weyers S 2007 *IEEE Trans. Instrum. Meas.* **56** 660–3
[57] Joyet A 2011 Résumé de l'estimation du Rabi pulling dû aux transitions $m = 1$ *Technical Report* Laboratoire Temps-Fréquence, Neuchâtel
[58] Lee H S, Kwon T Y, Kang H S, Park Y H, Oh C H, Park S E, Cho H and Minogin V G 2003 *Metrologia* **40** 224–31
[59] Bauch A, Achkar J, Bize S, Calonico D, Dach R, Hlavać R, Lorini L, Parker T, Petit G, Piester D, Szymaniec K and Uhrich P 2006 *Metrologia* **43** 109–20